Cell

Glucose dissociates DDX21 dimers to regulate mRNA splicing and tissue differentiation

Graphical abstract

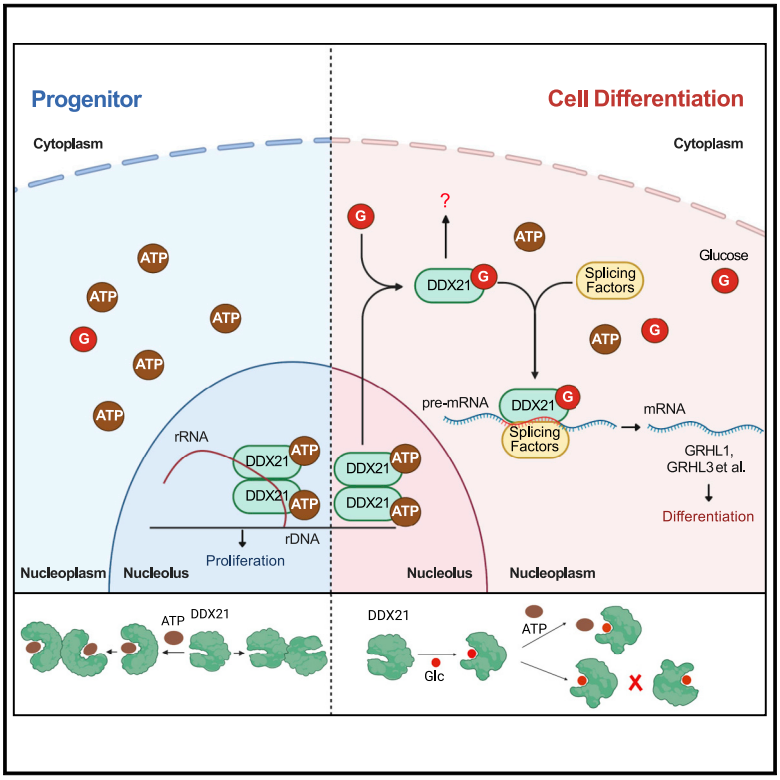

Highlights

- Glucose directly binds to the DDX21 ATP-binding domain and dissociates DDX21 dimers
- DDX21 monomers exit the nucleolus to integrate into nuclear RNA processing complexes
- DDX21 regulates tissue differentiation in an ATPase-independent manner
- DDX21 binds splicing factors to regulate splicing of key pro-differentiation genes

Authors

Weili Miao, Douglas F. Porter, Vanessa Lopez-Pajares, ..., Yinsheng Wang, Garry P. Nolan, Paul A. Khavari

Correspondence

khavari@stanford.edu

In brief

Glucose binds to DDX21 RNA helicase to modulate its role in splicing and promote epidermal differentiation.

Miao et al., 2023, Cell *186*, 80–97
January 5, 2023 Published by Elsevier Inc.
https://doi.org/10.1016/j.cell.2022.12.004

CellPress
OPEN ACCESS

Cell

Article

Glucose dissociates DDX21 dimers to regulate mRNA splicing and tissue differentiation

Weili Miao,[1,10] Douglas F. Porter,[1,10] Vanessa Lopez-Pajares,[1] Zurab Siprashvili,[1] Robin M. Meyers,[1] Yunhao Bai,[2] Duy T. Nguyen,[1] Lisa A. Ko,[1] Brian J. Zarnegar,[1] Ian D. Ferguson,[1,3] Matthew M. Mills,[4] Christie E. Jilly-Rehak,[4] Cheng-Guo Wu,[5] Yen-Yu Yang,[6] Jordan M. Meyers,[1] Audrey W. Hong,[1] David L. Reynolds,[1] Muthukumar Ramanathan,[2] Shiying Tao,[1] Sizun Jiang,[7] Ryan A. Flynn,[8] Yinsheng Wang,[6] Garry P. Nolan,[2] and Paul A. Khavari[1,3,9,11,*]

[1]Program in Epithelial Biology, Stanford University School of Medicine, Stanford, CA, USA
[2]Department of Pathology, Stanford University School of Medicine, Stanford, CA, USA
[3]Program in Cancer Biology, Stanford University, Stanford, CA, USA
[4]Department of Earth System Science, Stanford University, Stanford, CA, USA
[5]Molecular and Cellular Physiology, Stanford University School of Medicine, Stanford, CA, USA
[6]Department of Chemistry, University of California, Riverside, CA, USA
[7]Center for Virology and Vaccine Research, Beth Israel Deaconess Medical Center, Boston, MA, USA
[8]Department of Stem Cell and Regenerative Biology, Harvard University, Cambridge, MA, USA
[9]Veterans Affairs Palo Alto Healthcare System, Palo Alto, CA, USA
[10]These authors contributed equally
[11]Lead contact
*Correspondence: khavari@stanford.edu
https://doi.org/10.1016/j.cell.2022.12.004

SUMMARY

Glucose is a universal bioenergy source; however, its role in controlling protein interactions is unappreciated, as are its actions during differentiation-associated intracellular glucose elevation. Azido-glucose click chemistry identified glucose binding to a variety of RNA binding proteins (RBPs), including the DDX21 RNA helicase, which was found to be essential for epidermal differentiation. Glucose bound the ATP-binding domain of DDX21, altering protein conformation, inhibiting helicase activity, and dissociating DDX21 dimers. Glucose elevation during differentiation was associated with DDX21 re-localization from the nucleolus to the nucleoplasm where DDX21 assembled into larger protein complexes containing RNA splicing factors. DDX21 localized to specific SCUGSDGC motif in mRNA introns in a glucose-dependent manner and promoted the splicing of key pro-differentiation genes, including *GRHL3*, *KLF4*, *OVOL1*, and *RBPJ*. These findings uncover a biochemical mechanism of action for glucose in modulating the dimerization and function of an RNA helicase essential for tissue differentiation.

INTRODUCTION

The stratified epithelium of cutaneous epidermis forms the outer barrier of the skin where it protects against external environmental impacts.[1–3] The epidermis encompasses distinct layers of keratinocytes derived from mitotically active basal cells adherent to the cutaneous basement membrane. Post-mitotic differentiating suprabasal cells generate the proteins and lipids essential for cutaneous barrier formation in the stratum corneum.[4] Disruptions in this process contribute to the common skin diseases[5] as well as to the monogenic diseases that arise from disruptions in >85 genes essential for epidermal differentiation. The expression of ~3,500 genes changes during epidermal differentiation[6]; however, roles for small biomolecular cues in this process, as well as the proteins they may modulate, are not fully characterized.

Glucose is an abundant monosaccharide that serves as a major energy source for cellular function. ATP produced via glucose metabolism supports diverse activities, including enzymatic biosynthesis, intracellular transport, and cellular proliferation. A recent study[7] indicated that glucose accumulates in differentiated cells in several tissues, including the epidermis where it is essential for differentiation. Differentiation-associated glucose accumulation occurred without increased metabolism, and glucose depletion by genetic and pharmacologic means was rescued by non-metabolizable glucose analogs, indicating that glucose itself acts as a biomolecular cue that enables the differentiation process. Consistent with this, glucose directly bound the pro-differentiation transcription factor Interferon Regulatory Factor 6 (IRF6) and enhanced differentiation gene induction.[7] These observations indicate that direct glucose binding may remodel the function of proteins essential for differentiation and provide a rationale to search for additional glucose binding proteins affecting cell state transitions.

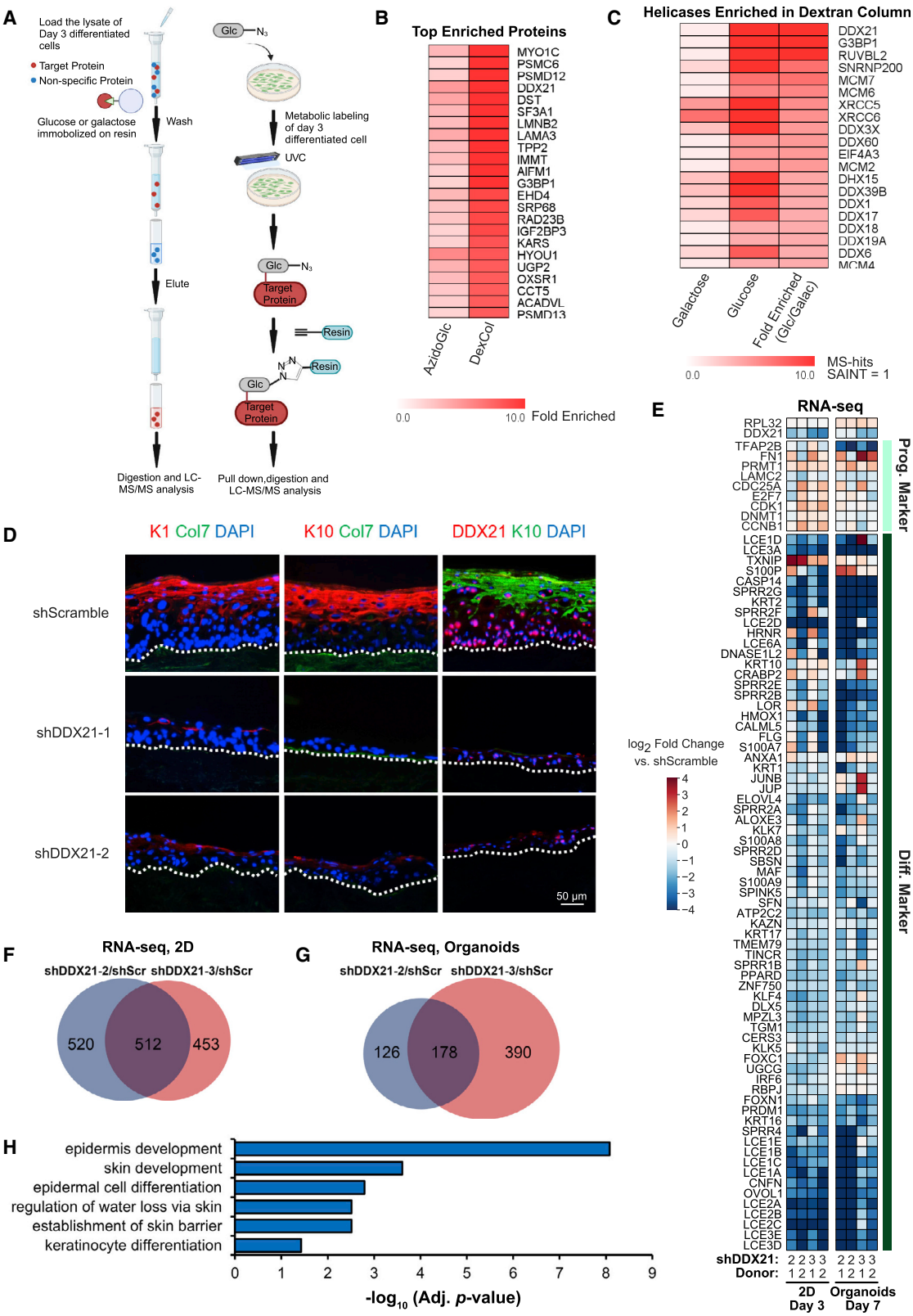

(legend on next page)

DDX21, a DEAD-box RNA helicase, uses the energy from ATP hydrolysis to catalyze the unwinding of structured RNAs, the separation of RNA duplexes and the remodeling of RNA-protein complexes.[8] DDX21 is implicated in many cellular processes, including ribosomal RNA processing[9] and RNA polymerase II (RNA Pol II)-mediated transcription.[10] DDX21, binding to 7SK RNA within the 7SK small nuclear ribonucleoprotein particle (snRNP) complex, is recruited to the promoters of RNA Pol II-transcribed genes encoding ribosomal proteins and snoRNAs in the nucleoplasm.[9] Notably, DDX21 also influences c-Jun[11] transcriptional activities, suggesting additional potential roles in gene expression. Due to its important function in ribosome biogenesis and general transcription, DDX21 alterations are strongly correlated with multiple diseases, including breast cancer,[8,12] gastric cancer,[13] and melanoma.[14] Recent work also reported that DDX21 regulates melanocyte stem cell differentiation.[15] However, a function for DDX21 in epidermal differentiation has not yet been described.

Here, we show that glucose competes with ATP for direct binding to DDX21 and inhibits DDX21 helicase activity. An indispensable role for DDX21 was identified in epidermal tissue, where DDX21 was required for the normal induction of differentiation in a helicase-independent manner. Glucose binding impaired DDX21 dimerization and enabled DDX21 re-localization from the nucleolus to the nucleoplasm where it assembled into larger protein complexes containing splicing factors. Glucose elevation in epidermal differentiation altered DDX21 associations with RNA, targeting it to pro-differentiation mRNA introns at specific RNA motifs accompanied by altered splicing of essential pro-differentiation genes, including indispensable pro-differentiation transcription factors, such as *GRHL1-3*, *KLF4*, *OVOL1*, and *RBPJ*, along with differentiation-modulating signaling regulators, such as *JAG1* and *NOTCH3*. These data identify an essential role for glucose binding to DDX21 to remodel its interactors and enable differentiation in epidermis.

RESULTS

Glucose interacts with DDX21

Glucose was recently found to be elevated in post-mitotic differentiated cells of epidermal tissues by GFP glucose sensor[7] and nanoscale secondary ion mass spectrometry (NanoSIMS) (Figure S1A), where it proved essential for epidermal differentiation, in part via direct binding to the pro-differentiation transcription factor, IRF6.[7] Keratinocyte progenitor cell self-renewal, however, is not inhibited by glucose restriction (Figure S1B). To search for additional glucose-binding proteins with roles in differentiation, two MS-based experiments were performed. The first used affinity chromatography with the glucose polymer dextran to purify glucose-binding proteins, and the second used a click chemistry approach within intact cells[7] to identify proteins cross-linked to azido glucose by ultraviolet C (UVC) (Figure 1A). The two methods yielded an overlapping set of 91 proteins (Table S1); unexpectedly, most of these were RNA binding proteins (RBPs) (Figure S1C). Among RBPs, the DEAD-box RNA helicase DDX21 was the most enriched (Figure 1B). RNA helicases share a highly conserved structure[16] and 31 additional helicases were enriched in the glucose dextran column (SAINT = 1, Figure 1C and Table S1), suggesting that helicases may represent a previously unappreciated class of glucose-binding proteins.

DDX21 is essential for epidermal tissue differentiation

Given the recently noted requirement for glucose elevation in epidermal differentiation, the role of DDX21 in this process was explored. DDX21 impacts processes important for cell proliferation,[17] including rRNA processing and RNA Pol II-driven transcription.[9] Consistent with this, DDX21 depletion decreased expression of hallmark progenitor genes and slowed keratinocyte progenitor proliferation *in vitro* (Figures S1D and S1E). Surprisingly, DDX21 loss also impaired induction of epidermal differentiation genes *in vitro* as well (Figure S1F). To examine the function of DDX21 within 3D tissue, DDX21 depletion was performed in organotypic human skin tissue.[6,18–20] DDX21 loss decreased proliferation and epidermal thickness in the absence of signs of enhanced cell death, while reducing differentiation gene expression (Figures 1D–1H and S1G–S1L). These data suggest an essential role for DDX21 in epidermal differentiation.

Glucose binds the DDX21 ATP-binding domain

In light of the data supporting an essential role for both glucose and DDX21 in epidermal differentiation, the interaction of glucose and DDX21 was next examined. Microscale thermophoresis (MST) and fluorescence quenching (FQ)[21,22] demonstrated binding between purified recombinant human DDX21 protein and glucose (Figures 2A, S2A, and S2B) (K_d = 3.26 μM for MST, K_d = 0.18 μM for FQ); galactose, a glucose stereoisomer with chirality distinct from glucose, lacked comparable binding (Figure S2C). The non-metabolizable glucose analog, 3-O-methyl-D-glucose (3OMG), which can rescue impaired epidermal differentiation due to glucose restriction,[7] bound DDX21 at similar affinity to glucose (K_d = 3.98 μM, Figure S2C). These data indicate that DDX21 directly binds glucose as well

Figure 1. Glucose binds to DDX21 and DDX21 is essential for epidermal differentiation

(A) Workflow for the discovery of glucose binding proteins by MS using either dextran column (left) or azido glucose (right).

(B) Heatmap of the top enriched proteins among the 91 commonly enriched proteins.

(C) Heatmap of the top enriched helicases in the dextran column.

(D) Keratin 1 (K1), Keratin 10 (K10), DDX21, and Collagen VII (Col7) staining in skin tissue organoids comparing DDX21 shRNA with control shRNA; dotted line, basement membrane.

(E) Changes in progenitor and differentiation markers upon DDX21 loss in differentiated cells and skin tissue organoids (RNA-seq); differentiation genes shown include all genes with a GO term of keratinocyte differentiation, regulation of keratinocyte differentiation, or keratinization, with an FDR <0.05 in ≥4 biological replicates.

(F and G) Venn diagram showing the overlap of downregulated genes (FDR < 0.05) between the two shDDX21 in RNA-seq of differentiated cells (F) and organotypic human epidermal tissue (G).

(H) Adjusted p values of biological process GO terms for RNAs downregulated in RNA-seq of organotypic human epidermal tissue (178 genes from G).

See also Figure S1 and Table S1.

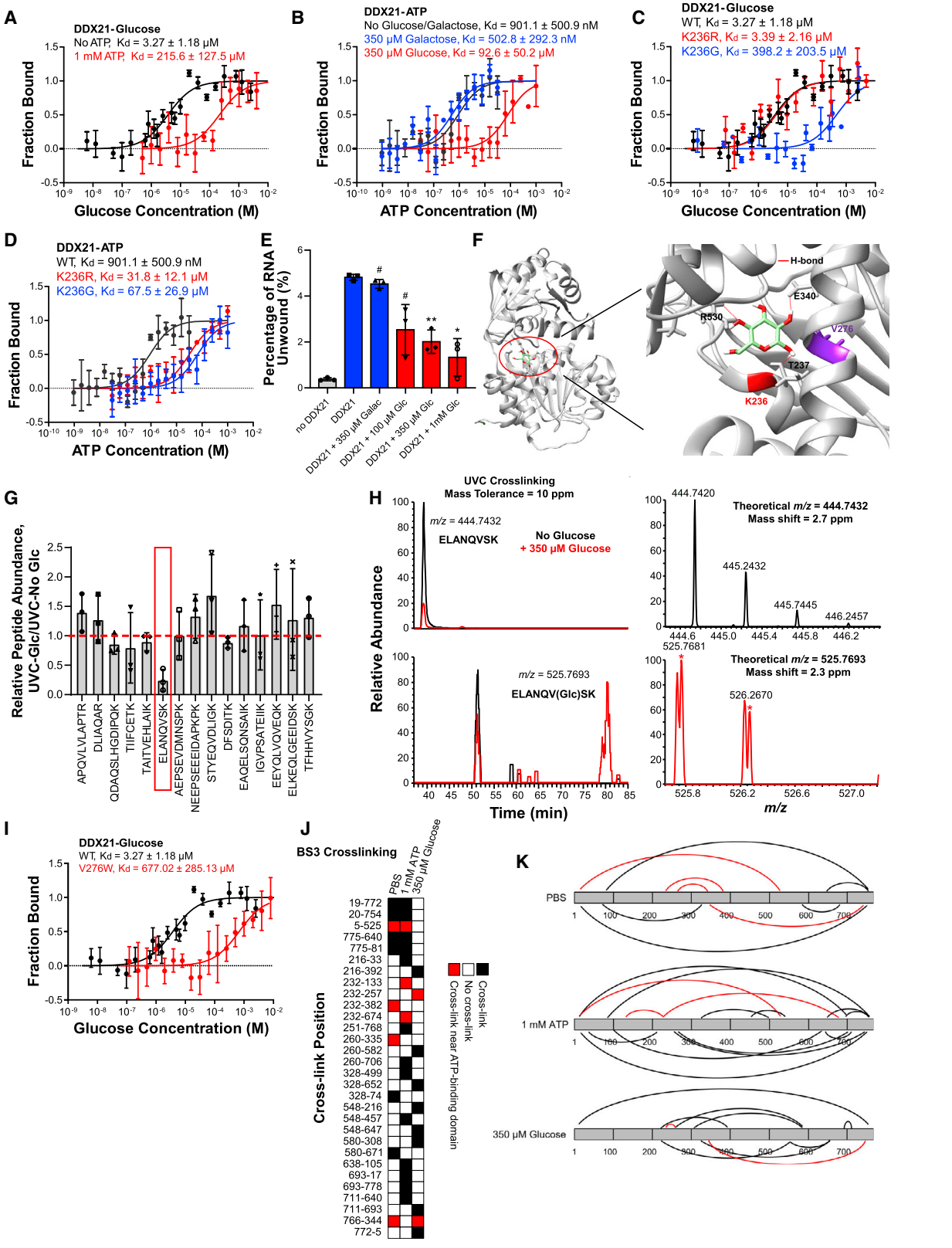

(legend on next page)

as a non-metabolizable glucose analog that is functional in epidermal differentiation.

A feature of DDX21 shared by other RNA helicases is ATPase activity, which uses ATP hydrolysis to unwind RNA.[16] The addition of 350 μM glucose, the physiological concentration of glucose in differentiated keratinocytes,[7] decreased DDX21 binding to ATP by two orders of magnitude and vice versa (Figures 2A and 2B). Galactose failed to alter DDX21's association with ATP (Figure 2B). DDX21 ATPase activity, moreover, was modestly reduced in the presence of glucose (Figure S2D). These findings suggest that glucose and ATP compete for binding to DDX21.

Regions of the DDX21 protein responsible for glucose binding were next studied, beginning with the DDX21 ATP-binding domain. Analysis of the crystal structure of DDX21 bound to the ATP analog, AMPPNP,[23] suggested that the sequence 231–236 (RTGTGK) may be important for AMPPNP binding (Figure S2E). MST analysis demonstrated that AMPPNP bound DDX21 at comparable affinity to ATP (Figure S2F), consistent with a shared potential binding site. Previous reports indicated that K236 within the DDX21 ATP-binding site is important for ATPase activity.[12] Therefore, K236 was substituted with either a charge-conservative arginine (K236R) or with glycine (K236G) (Figure S2G). Unlike wild-type (WT) DDX21, neither $DDX21^{K236R}$ nor $DDX21^{K236G}$ displayed ATPase activity (Figure S2D), but $DDX21^{K236R}$ still bound glucose, whereas $DDX21^{K236G}$ did not (Figure 2C). As expected, both mutants displayed reduced affinity for ATP (Figure 2D). The binding affinity of $DDX21^{K236R}$ toward glucose was not perturbed by ATP, for which it no longer had affinity (Figure S2H). Consistent with glucose binding to the ATP-binding domain, the RNA unwinding activity of DDX21 was reduced by glucose but not by galactose (Figure 2E). These data suggest that DDX21 binding to glucose requires sequences within its ATP-binding domain and establishes specific point mutants in that domain that distinguish glucose and ATP binding.

The glucose binding site on DDX21 was next further localized. First, molecular docking[24,25] was performed with glucose and DDX21. All top five structures placed glucose in the ATP-binding domain of DDX21, with the best predicted binding free energy of −7.3 kcal/mol (Figure 2F), a level considered indicative of a "valid" binding event.[26] Second, UVC crosslinking-MS of recombinant DDX21 protein (Figure S2I) found a single peptide, ELANQVSK, crosslinked with glucose at valine 276 (V276) with clear selected ion chromatography (SIC), MS, and MS/MS (Figures 2G, 2H, and S2J). The position of V276 is within the DDX21 ATP-binding domain (Figure 2F). The peptide APQVLVLAPTR, which is at the N-terminal side of the target peptide, served as a representative negative control where no glucose crosslinked peptides were found (Figure S2K). Further mutating the V276 to an amino acid with a bulky side chain, tryptophan (W), to occupy the binding domain and sterically block interactions, strongly reduced DDX21's affinity for glucose and ATP (Figures 2I, S2L, and S2M). These data suggest that glucose associates with the DDX21 ATP-binding domain.

To explore whether the presence of glucose is associated with a conformational change in DDX21, crosslinking MS (CLMS) was performed (Figure S2N). CLMS found consistent crosslinking sites, with more crosslinking sites identified in the ATP binding state, and glucose binding induced a substantially different crosslinking pattern (Figures 2J and 2K). Together, these results demonstrate that glucose binds to the ATP-binding domain of DDX21 and alters DDX21 protein conformation.

Glucose inhibits DDX21 dimerization

Glucose impacts on DDX21 conformation were further explored, particularly with respect to its dimerization. DDX21 dimerization is essential for its helicase activity and depends upon its hydrophobic LAAALA sequence.[27] To generate an obligate DDX21 monomer, LAAALA amino acids 611–616 of DDX21 were mutated to RRRRRR (termed $DDX21^{611R}$); an LAAALA deletion construct was also generated (termed $DDX21^{611Del}$) (Figure S3A). Robust dimerization occurred with WT DDX21 protein (K_d = 13.8 nM), which was reduced >5-fold by both glucose and 3OMG, but not by galactose (Figures 3A, S3A, and S3B). The helicase-dead $DDX21^{K236R}$ dimerization was comparable with WT and also inhibited by glucose (Figures 3B and S3C); as expected, dimerization was dramatically reduced for $DDX21^{611R}$ dimerization domain mutant (Figure 3B). Co-immunoprecipitation and blue native gels further suggested the inhibition of DDX21 dimerization by glucose (Figures 3C and S3D–S3I). In live keratinocyte progenitor cells, strong DDX21 dimerization

Figure 2. Glucose binds to the ATP binding site of DDX21 and changes DDX21 protein conformation

(A) MST of DDX21's binding affinity for glucose ±1 mM ATP.

(B) MST of DDX21 binding to ATP ±350 μM glucose or galactose.

(C) MST of glucose binding to DDX21 WT, K236R, and K236G mutants.

(D) MST of ATP-binding affinities of DDX21 WT, K236R, and K236G mutants.

(E) Helicase activity of DDX21 ±galactose or ±glucose.

(F) Molecular docking by UCSF Chimera shows the predicted binding site of glucose to DDX21 (PDB: 6L5N).

(G) Relative abundance of the peptides with no glucose modification, calculated from the intensity obtained from 350 μM glucose/no-glucose, both with UVC crosslinking (top 15 most abundant peptides).

(H) Selected ion chromatography (SIC) and MS of the targeted peptide of DDX21 (ELANQVSK) with (red) or without (black) glucose incubation during UVC crosslinking. 10 ppm mass tolerance was applied to plot SIC. *MS peak for the glucose crosslinked peptide.

(I) MST analysis of glucose binding to DDX21 WT and V276W mutant.

(J and K) BS3-induced protein sites crosslinked in PBS, 1 mM ATP or 350 μM glucose. Crosslinking sites within 5 amino acids are marked as the same site. The black lines and boxes in the diagram represent BS3-induced crosslinks within DDX21 and the red lines and boxes highlight the crosslinks near ATP-binding domain of DDX21.

Error bars, standard deviations from ≥3 biological replicates. p values, two-tailed Student's t test or Welch's t test.

See also Figure S2.

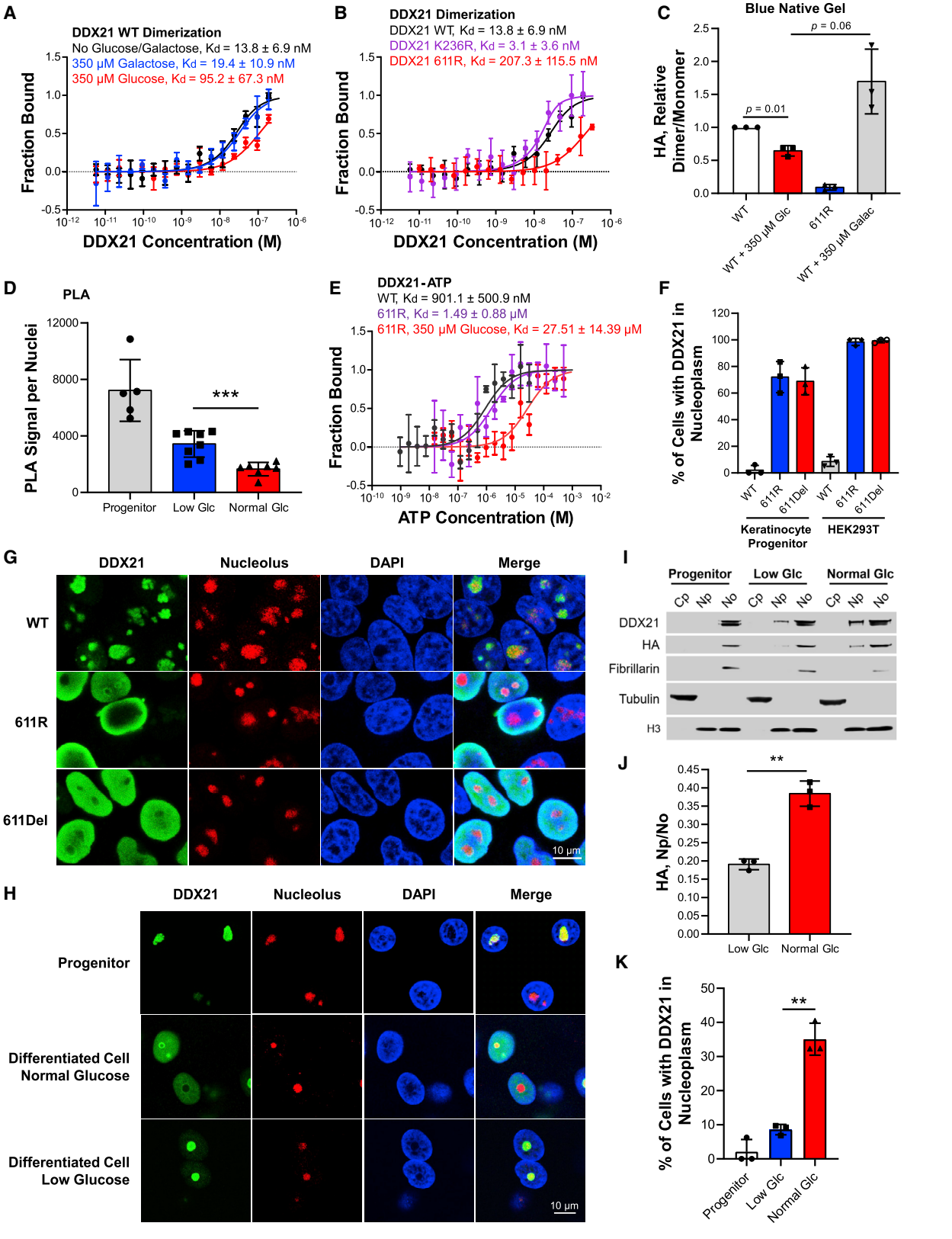

(legend on next page)

signal, measured by proximity ligation assay (PLA), was observed predominantly in the nucleolus; with increased cellular glucose concentration during differentiation, fewer dimers were observed (Figures 3D and S3J). Dimerization-defective DDX21^{611R} displayed similar affinities as WT DDX21 for both ATP and glucose (Figures 3E and S3K), suggesting that dimerization is not necessary for ATP or glucose binding by DDX21. As with WT DDX21, glucose binding also inhibited ATP binding for DDX21^{611R} (Figure 3E).

DDX21 monomers localize in the nucleoplasm

DDX21 is located predominantly in the nucleolus[28]; however, the localization of monomeric DDX21 is unknown. Immunofluorescence suggested a nucleolus-localization of WT DDX21, in contrast to DDX21^{611R} obligate monomers, which were primarily in the nucleoplasm (Figures 3F, 3G, and S3L).

The observed disruption of DDX21 dimers by glucose raised the possibility that glucose-induced DDX21 monomers might also facilitate a re-distribution of DDX21 from the nucleolus to the nucleoplasm. Accordingly, this possible re-localization was examined for WT DDX21 in the context of the physiologic increase in intracellular glucose that occurs during epidermal progenitor differentiation.[7] Epidermal progenitor cells, which have low levels of intracellular glucose, predominantly displayed nucleolar DDX21. Differentiated cells, which elevate intracellular glucose levels to 350 μM, in contrast, displayed increased amounts of nucleoplasmic DDX21, which could be blocked by glucose restriction (Figures 3H–3K). Strikingly, the localization of the DDX21^{K236G} mutant, which does not bind glucose, was not regulated by glucose elevation during differentiation (Figures S3M and S3N). The re-localization of DDX21 was also observed in skin tissue organoids (Figure S3O). These data are consistent with a model in which DDX21 re-localizes from the nucleolus to the nucleoplasm in the setting of glucose-facilitated monomerization.

In light of DDX21's localization to the nucleoplasm and its coordination with RNA Pol II,[9] the impact of glucose on DDX21 genomic association was examined. CUT&RUN[29] found gene promoters (e.g., *USP5* and *CEP290*) enriched in DDX21 binding, as reported,[9] however, not significantly regulated by glucose (Figure S3P and Table S2). Meanwhile, the proportion of DDX21 co-purified with chromatin was unaffected by glucose (Figure S3Q), arguing against a major role for glucose in modulating DDX21 associations with the genome.

DDX21-enabled differentiation is ATPase-independent and requires glucose binding

Since DDX21 is mainly nuclear, the subcellular levels of glucose and ATP were next explored as a function of differentiation. NanoSIMS, which enables nanoscale resolution measurements of the elemental and isotopic composition of cells, was used with both isotopically labeled glucose and ATP. A high abundance of ATP was detected in the nucleus of progenitor cells, whereas differentiated cells displayed less abundant detectable ATP (Figures 4A, 4B, and S4A). Glucose displayed the opposite pattern: low in undifferentiated cells and increased in both the nuclear and cytoplasmic compartments of differentiated cells (Figures 4A, 4B, and S4A), consistent with its elevation in suprabasal layers in tissue organoids (Figure S1A). These findings are consistent with the observation that glucose supplants ATP binding to DDX21 during differentiation and that ATP-binding may not be necessary for DDX21's function in differentiation. Notably, when overexpressing WT DDX21 and DDX21^{K236R} in progenitor cells, the ATP-binding deficient, helicase-dead mutant DDX21^{K236R} drove differentiation (Figure S4B), indicating that DDX21 ATPase activity is not required in differentiation.

To further explore the function of DDX21's ATPase activity and glucose binding in epidermal differentiation, rescue experiments were performed in cultured cells and tissue organoids (Figure S4C). In cultured cells, helicase-dead mutant DDX21^{K236R} effectively rescued the impaired differentiation induced by DDX21 knockdown, whereas WT DDX21 and dimerization mutant DDX21^{611R} exhibited partial rescue; glucose binding-deficient DDX21^{V276W} did not rescue (Figure S4D). In skin tissue organoids, helicase-dead mutant DDX21^{K236R} and dimerization mutant DDX21^{611R} also rescued differentiation, WT DDX21 partially rescued, and glucose-binding DDX21 mutants failed to rescue (Figures 4C and 4D). These results support a model in which glucose binding, but not ATPase activity, is essential for DDX21-enabled differentiation. Interestingly, only WT DDX21, but not the helicase-dead or dimerization mutants, rescued the expression of proliferation marker Ki67 in progenitor cells of tissue organoids (Figures S4E and S4F), suggesting that the ATPase activity of DDX21 is essential to maintain progenitor cell proliferation.

These observations were recapitulated via gene editing to introduce specific point mutations at the endogenous *DDX21* locus. Adeno-associated virus (AAV)/CRISPR-Cas9 homology-directed recombination (HDR) achieved 75%–98% editing of

Figure 3. Glucose inhibits DDX21 dimerization and re-localizes DDX21 to the nucleoplasm

(A) MST of DDX21 dimerization ±350 μM glucose or galactose.
(B) MST of the effects of DDX21 mutations on DDX21 dimerization.
(C) The dimer/monomer ratio of DDX21 ±350 μM glucose or galactose, as obtained from HA western blot analysis of blue native gels.
(D) PLA signal for the interaction between FHH-DDX21 and V5-DDX21 (dimerization) in progenitor, differentiated cells maintained in low or normal glucose.
(E) MST of dimerization mutant DDX21^{611R} binding to ATP ±350 μM glucose.
(F) Percentage of cells with DDX21 WT or dimerization mutants localized in the nucleoplasm in HEK293T or keratinocyte progenitors.
(G) Immunofluorescence of HA-DDX21 WT and dimerization mutants in HEK293T cells.
(H) Immunofluorescence of HA-DDX21 in keratinocyte progenitor, differentiated cells grown in normal or low glucose. Green, anti-HA signal.
(I) Western blot of nucleolus fractionation in progenitor, differentiated cells grown in normal or low glucose. Cp, cytoplasm; Np, nucleoplasm; and No, nucleolus.
(J) Relative FHH-DDX21 abundance in the nucleoplasm (Np)/nucleolus (No) from western blot.
(K) Percentage of cells with nucleoplasmic FHH-DDX21 in three conditions: progenitor keratinocytes, differentiated cells grown in low or normal glucose.
Error bars, standard deviations from ≥3 biological replicates. p values, two-tailed Student's t test or Welch's t test.
See also Figure S3.

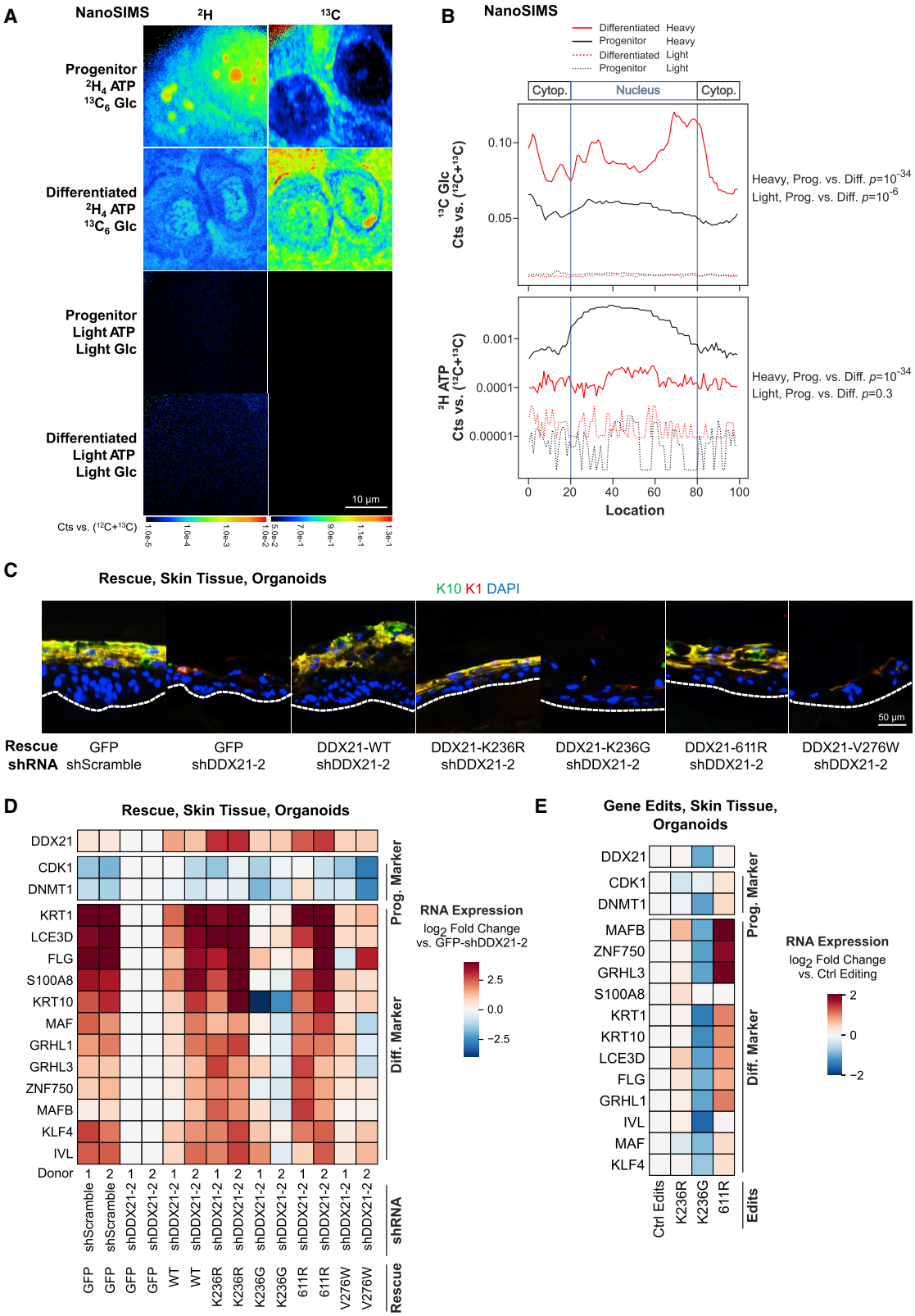

(legend on next page)

native *DDX21* alleles in bulk populations of normal human keratinocytes (Figure S4G). In reconstituted skin organoid tissue, eliminating DDX21 helicase activity via introduction of the K236R substitution failed to impair epidermal differentiation, as did the dimerization mutation 611R. The K236G glucose-binding deficient *DDX21* mutation, in contrast, abolished differentiation (Figure 4E). This *in situ* gene editing data further support a model in which DDX21-enabled differentiation requires glucose binding but not helicase activity or dimerization.

Glucose elevation is associated with DDX21 assembly in larger protein complexes

Glucose binding is necessary for DDX21's function in differentiation, likely partially though re-distributing the protein from the nucleolus to the nucleoplasm, which might alter DDX21's protein interactions. Fast protein liquid chromatography (FPLC) fractionation[30] detected DDX21 across a range of molecular weight fractions, in potential agreement with the premise that it resides in multiple protein-protein contexts (Figures 5A, S5A, and S5B). Incubating protein fractions with 350 μM glucose shifted DDX21 into larger protein complexes (Figures 5A, 5B, and S5B–S5D). Immunoblotting for HNRNPC confirmed that glucose did not cause global shifts in RBP distribution and that elution volume was stable between runs (Figure S5E). These results indicate that glucose enables the incorporation of DDX21 into larger protein assemblies.

Glucose increases DDX21 proximity to RNA splicing factors

To identify the proteins whose adjacency to DDX21 is modulated by glucose, proximal proteomics (BioID)[31] was applied. DDX21 was fused to the *Bacillus subtilis* biotin ligase (BASU)[32] and expressed in primary human epidermal keratinocytes (Figures S5F and S5G). Three cellular conditions were studied, each of which supports healthy cell viability[7]: (1) undifferentiated keratinocyte progenitors, which contain lower levels (135 μM) of intracellular glucose; (2) keratinocytes differentiated via confluence and elevated calcium, grown in normal glucose media (4.5 g/L, 25 mM); these cells elevate their intracellular glucose levels to 350 μM; and (3) keratinocytes differentiated in glucose-restricted media (0.5 g/L, 2.8 mM), which display intracellular glucose concentrations similar to progenitor cells. BioID analyses identified ~300 DDX21 proximal proteins in each condition (Figures 5C, S5H and Table S3), with selected interactors validated by western blot (Figure S5G). 143 DDX21-proximal proteins were detected in all three conditions; however, the rest differed between conditions, indicating that glucose alters the spectrum of proteins adjacent to DDX21.

The 67 DDX21 proximal proteins identified in differentiated cells grown in normal glucose media were enriched for gene ontology (GO) terms associated with the nuclear body, spliceosome, and autolysosome (Figures 5D and S5I). In contrast, the 194 proteins enriched in progenitor and differentiated cells grown in low glucose media associated with terms for the nucleolus and ribosomes (Figures 5D and S5J). Known DDX21 interactors, such as DDX50 and NOP56, were enriched in both conditions, helping validate the dataset (Figure 5E). Specific nucleolar proteins, such as NOLC1 and PPAN, were more enriched with glucose restriction, whereas multiple RNA splicing factors showed greater enrichment in the cells supplied with normal glucose (Figures 5E and S5K). The interactions between DDX21 and splicing factors (e.g., HNRNPUL1 and HNRNPA2B1) in differentiated keratinocyte cells maintained in normal glucose was confirmed by PLA (Figure S5L). Consistent with this, GO analysis of biological processes terms indicated that rRNA processing was more enriched in low glucose, whereas mRNA splicing was more enriched in normal glucose (Figures 5F and 5G). Interestingly, GO analysis of $DDX21^{K236R}$ proximal proteins in HEK293T cells revealed greater enrichment of splicing factors compared with WT DDX21 protein (Figures S5M and S5N), suggesting that DDX21's interaction with splicing factors is helicase activity-independent. Immunoprecipitation of HA-tagged DDX21 resulted in a strong enrichment of HNRNPUL1, a target detected in BioID data, with a greater enrichment in differentiated cells cultured in normal glucose (Figures 5H and 5I). In addition, DDX21 was shifted into larger molecular weight elution fractions in differentiated cells cultured in normal glucose (Figures 5J, S5O, and S5P), consistent with its possible incorporation into pre-mRNA processing complexes. These data suggest that glucose facilitates DDX21 proximity to proteins involved in mRNA processing.

Glucose enhances DDX21 association with mRNA introns

The impact of glucose on DDX21 RNA interactions was next examined. RNA crosslinking followed by immunoprecipitation (CLIP, specifically easyCLIP-seq)[33] demonstrated a similar DDX21 crosslinking rate to RNA in differentiated cells maintained in either normal or low glucose, indicating that glucose levels do not globally alter the fraction of DDX21 bound to RNA

Figure 4. DDX21-enabled differentiation is ATPase-independent and requires glucose binding

(A) NanoSIMS of ^{13}C and ^{2}H in progenitor and differentiated keratinocytes cultured with $^{13}C_6$ glucose and $^{2}H_4$ ATP (top two rows) or light glucose and ATP (bottom two rows). Intensities represent the relative counts normalized to total carbon counts ($^{12}C+^{13}C$).

(B) Relative counts normalized to total carbon counts ($^{12}C+^{13}C$) for ^{2}H and ^{13}C in progenitor and differentiated cells. The nucleus was defined by ^{31}P signal that was collected simultaneously.

(C) Keratin 1 (K1, red) and Keratin 10 (K10, green) staining in organotypic human epidermal tissue, comparing DDX21 shRNA with control shRNA and DDX21 shRNA with WT or mutant DDX21 rescue; dotted line, basement membrane.

(D) qPCR of progenitor and differentiation markers in control shRNA, DDX21 shRNA, and DDX21 shRNA with WT or mutant DDX21 rescue in organotypic human epidermal tissue. Data are normalized to DDX21 shRNA with GFP control.

(E) qPCR of progenitor and differentiation markers in primary keratinocytes after gene editing at the endogenous *DDX21* gene locus with K236R, K236G, and 611R mutations, grown as organotypic human epidermal tissue. Data represent the mean from ≥2 replicates. Mutants are normalized to their respective control edit; that is, K236K for K236R and K236G and 611LAAALA for 611RRRRRR.

See also Figure S4.

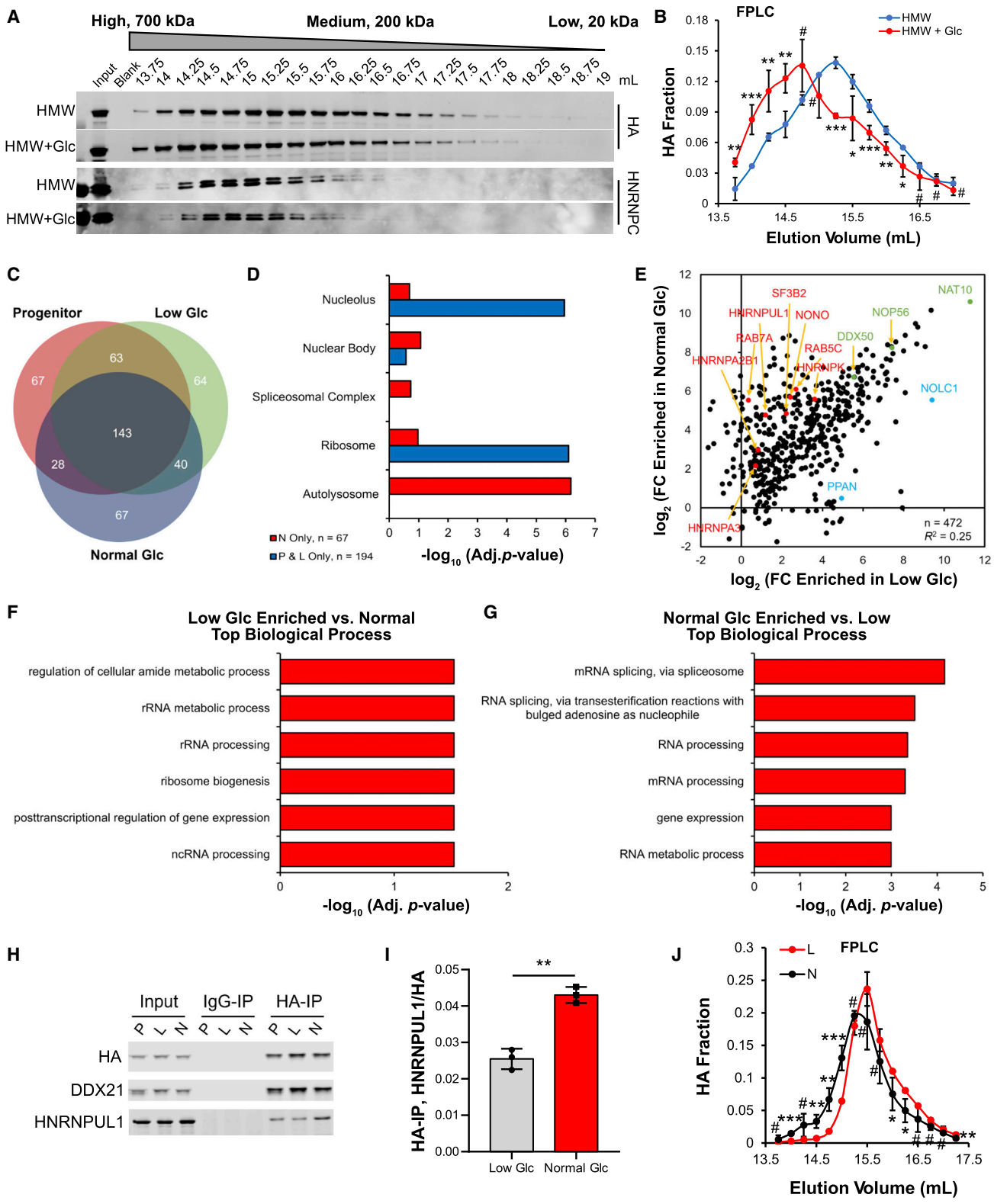

Figure 5. Glucose transitions DDX21 into a larger complex containing RNA splicing factors

(A) Western blot of HA-DDX21 and HNRNPC in FPLC from 13.75 to 19 mL ±350 μM glucose incubation in the high molecular weight (HMW) fraction.

(B) Distribution of DDX21 protein in FPLC, ±350 μM glucose in the HMW fraction from western blot.

(legend continued on next page)

(Figures S6A and S6B). Unexpectedly, CLIP-seq data identified a specific SCUGSDGC RNA motif as highly enriched at sites of DDX21 binding across the transcriptome (Figure 6A), with an alternative analysis for pre-mRNA identifying a GGC-repeat motif (Figure S6C). *In vitro*, recombinant DDX21 protein bound an RNA matching the CLIP-seq DDX21 binding motif at 7-fold higher affinity than to G-quadruplex RNA (G4 RNA, Figure 6B), the best currently known DDX21-binding RNA,[34] suggesting the CLIP-seq identified motif may represent a natural DDX21 binding sequence and that the CLIP landscape is at least partially driven by DDX21's own RNA specificity. No binding was detected for an RNA with a random sequence (Figure 6B). DDX21 binding to both the CLIP-seq identified RNA motif and G4 RNA *in vitro* was not substantially altered by glucose (Figures 6B and S6D), indicating that glucose does not globally control the capacity of DDX21 to associate with RNA.

Analysis of CLIP-seq data indicated that DDX21 migrated from pre-rRNA to mRNA in order: (1) keratinocyte progenitors to (2) differentiated cells maintained in low glucose and to (3) differentiated cells cultured in normal glucose (Figures 6C and S6E). More importantly, DDX21 bound more to RNA introns in differentiated keratinocytes maintained in normal glucose than in progenitors or low glucose cells (Figures 6D, S6F, and Table S4). *JUP* and *GRHL3* RNAs are examples: in differentiated keratinocytes, DDX21 was crosslinked more to *JUP* and *GRHL3* introns in normal glucose, with little differential exon binding (Figure 6E). Furthermore, DDX21 binding migrated from U3 snoRNA (rRNA processing) to U1 snRNA (RNA splicing) with increased cellular glucose concentration (Figure 6F). Taken together, these results support a model wherein DDX21 reduces its role in rRNA processing upon differentiation with elevated glucose to play a potential role as a sequence-specific factor in pre-mRNA processing.

CLIP-seq data generated in HEK293T cells complemented these findings. They identified increased mRNA binding and reduced pre-rRNA binding for helicase-dead mutant DDX21^{K236R}, as well as dimerization domain mutant DDX21^{611R}, compared with WT DDX21 (Figure 6G and Table S4). This decreased binding to pre-rRNA is consistent with the observation that glucose binding and DDX21 dimer dissociation induced nucleolar exclusion (Figures 3F–3H). Increased binding to the splicing U1/U2/U6 snRNAs was observed for helicase-dead and dimerization DDX21 mutants (Figures 6H and S6G; Table S4). Taken together, these results indicated that glucose dissociates DDX21 dimers and reassembles DDX21 into complexes implicated in pre-mRNA processing.

DDX21 regulates mRNA splicing of epidermal differentiation genes

To explore possible DDX21 actions in glucose-regulated mRNA splicing across keratinocyte differentiation, mRNA splicing analyses of exon inclusion and intron retention were performed[35] (Table S5 and Table S6). Both analyses presented significant overlap of the differentially spliced mRNA across keratinocyte differentiation from progenitor to differentiated cells maintained in either low or normal glucose (Figure S7A). A comparison of mRNA splicing differences between normal and low glucose in differentiated cells to the CLIP-seq-identified DDX21 RNA binding differences in the same cohorts, also identified significant overlaps (Figure S7B). More importantly, exons upregulated by higher glucose showed significant differences in DDX21 binding on the −1 intron compared with the ±2 introns (Figure 7A). Introns immediately upstream of exons expressed higher in normal glucose had a significant increase in DDX21 binding with normal glucose compared with glucose restriction (Figure 7B), suggesting that glucose may enable DDX21 to bind to specific mRNA introns to promote mRNA splicing.

mRNA splicing changes caused by DDX21 depletion in differentiated cells were next examined. The most frequent splicing alteration caused by DDX21 loss, as identified by event-based alternative splicing quantification,[36] was exon skipping, which was also rescued by both WT DDX21 and DDX21^{K236R} (Figures 7C, S7C, and Table S7). Exons skipped upon DDX21 loss showed significant differences in DDX21 binding on the ±1 intron compared with the ±2 introns (Figure 7A). More strikingly, ±1 introns of exons skipped upon DDX21 loss had a significant increase in DDX21 binding under normal glucose compared with low glucose (Figure 7B), further supporting the role of glucose in DDX21-dependent splicing. Additionally, the DDX21 RNA binding motif (SCUGSDGC) was enriched in exons with increased exon inclusion (decreased exon skipping) in differentiated cells vs. progenitor; this was also observed in differentiated cells cultured in normal glucose vs. low glucose (Figure 7D). The SCUGSDGC DDX21 motif was especially enriched in these differentially skipped exon regions, even controlling for GC-bias (Figure S7D). These results suggest that RNA splicing during differentiation is regulated by DDX21 at least partially through the direct, glucose-dependent binding of DDX21.

Extracellular matrix protein 1 (ECM1)—a differentiation marker—has two splicing isoforms, a long isoform in basal keratinocytes (*ECM1a*) and a short isoform (*ECM1b*) found only in suprabasal keratinocytes and tonsils, which results from exon 7

(C) Overlap of enriched genes in progenitor, differentiated cell maintained in low or normal glucose in BioID hits, each normalized to their corresponding GFP control.
(D) Cell components enrichment in proteins from DDX21 proximal proteomes. P and L, proteins enriched only in progenitor and low glucose cells (n = 194); N, proteins enriched only in normal glucose cells (n = 67).
(E) Correlation between the DDX21/GFP enrichment ratios obtained via LC-MS/MS from low and normal glucose in differentiated cells among 472 total enriched genes.
(F and G) Adjusted p values of top biological process GO terms enriched in DDX21 proximal proteomes in low glucose compared with normal glucose (F) or normal glucose compared with low glucose (G).
(H) Western blot of HNRNPUL1 after HA-DDX21 immunoprecipitation in progenitor, differentiated cell grown in normal or low glucose.
(I) Relative enrichment of HNRNPUL1 in normal glucose compared with low glucose from western blot.
(J) Distribution of DDX21 FPLC from 13.75 to 17.25 mL in the HMW fraction in differentiated cells grown in normal or low glucose from western blot.
Error bars, standard deviations from ≥3 biological replicates. p values, two-tailed Student's t test.
See also Figure S5 and Table S3.

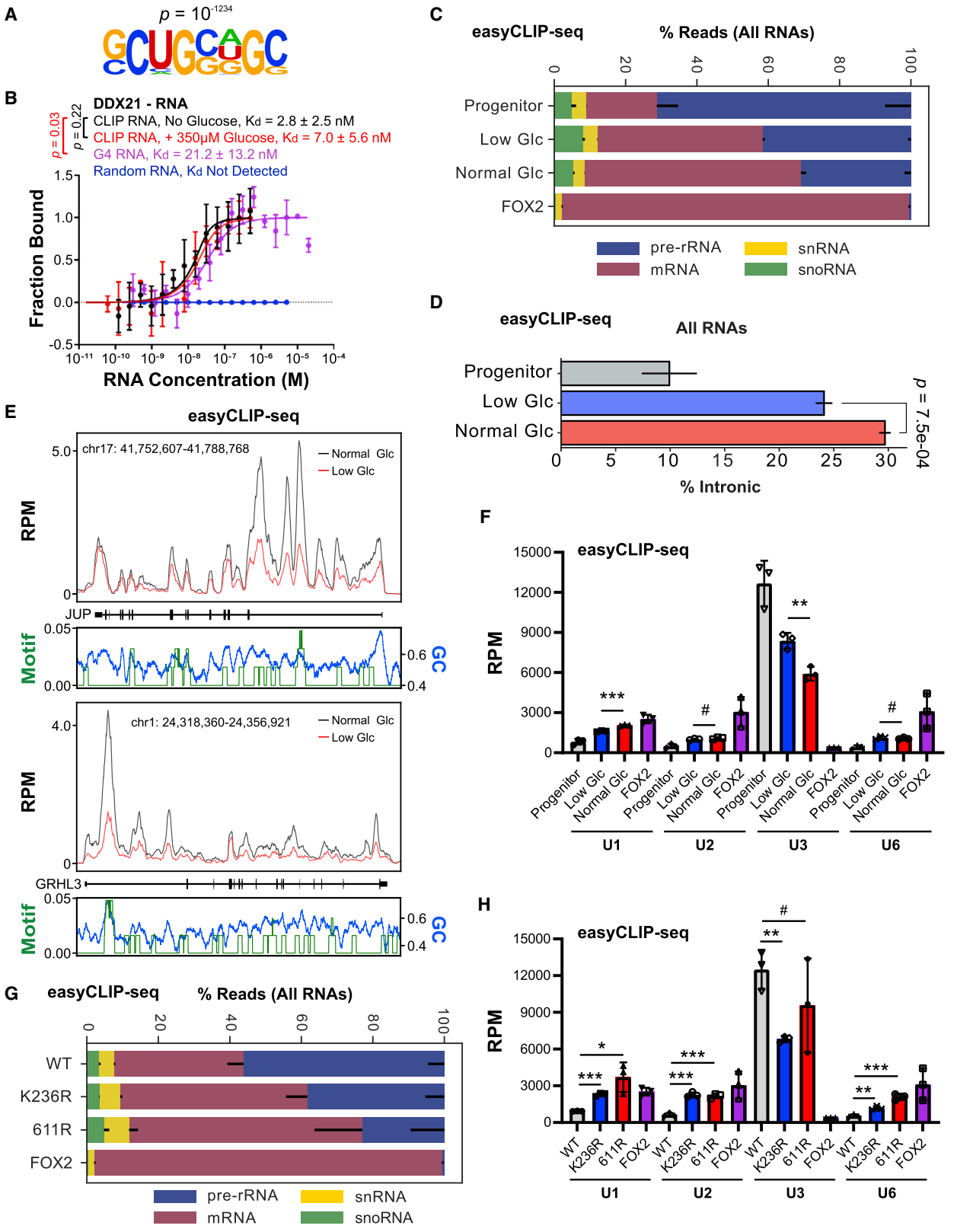

(legend on next page)

skipping of the long isoform.[37] ECM1 is implicated in keratinocyte homeostasis[38] and its mutation causes skin disease.[39] DDX21 loss resulted in a decrease in the differentiation-associated skipping of exon 7 in *ECM1* mRNA, which was rescued by both WT DDX21 and DDX21^{K236R} (Figures 7E and S7E). DDX21 bound strongly to the region around exon 7 in *ECM1* transcript in a glucose-dependent manner (Figure 7F), suggesting a role for DDX21 in promoting the exon 7 exclusion in *ECM1* mRNA and consistent with its glucose-dependent and helicase-independent action in this process.

mRNA splicing perturbations of exon inclusion and intron retention upon DDX21 loss were further assessed. Both exon inclusion and intron retention changes shared significant overlap with RNAs that display glucose-dependent DDX21-binding in CLIP-seq (Figure S7F). Reduced intron retention was observed in more differentiated cells (Figure S7G), suggesting that enhanced mRNA splicing or increased mRNA age in keratinocyte differentiation. 102 gene transcripts displayed glucose-dependent DDX21 association whose processing was also regulated by DDX21 (Figure S7F). These genes were enriched for GO terms related to skin development (Figure S7H) and include a variety of genes essential for normal epidermal differentiation and function, including *GRHL1-3*, *KLF4*, *OVOL1*, *RBPJ*, *JAG1*, and *NOTCH3*. Among these transcripts, differential exon usage was rescued by both the DDX21^{K236R} helicase-dead mutant and WT DDX21 (Figures 7G, S7C, and Table S7), further indicating that DDX21 regulates mRNA splicing independent of its helicase activity. For example, DDX21^{K236R} effectively rescued intron retention in *GRHL1* and *GRHL3* (Figure 7H), transcription factors essential for epidermal differentiation.[40–42] Meanwhile, strong separation of the *GRHL1* and *GRHL3* CLIP peaks between normal and low glucose conditions in differentiated cells was observed near the retained intron (Figure S7I), supporting the role of glucose in DDX21-dependent mRNA splicing of pro-differentiation factors, GRHL1 and GRHL3. Such intron retention events can affect differentiation: the overexpression of GRHL3 greatly induced differentiation, whereas overexpressing intron 13-retained GRHL3—an intron with increased retention upon DDX21 loss (Figure 7H and Table S7)—did not induce differentiation (Figure 7I). These results identify DDX21's role in regulating the splicing of differentiation-promoting mRNAs.

DISCUSSION

Here, we show that glucose directly binds a variety of RBPs and specifically controls the localization and function of the DDX21 DEAD-box RNA helicase in an essential role for DDX21 in mammalian tissue differentiation. In this setting, glucose elevation acts as a differentiation-induced cue to control DDX21 actions. DDX21 was found to be essential for epidermal tissue differentiation in a helicase-independent fashion, and direct glucose binding competed with ATP, induced conformational changes in the DDX21 protein, and dissociated its dimers. DDX21 monomers re-localized from the nucleolus to the nucleoplasm where they assembled into larger molecular weight complexes with RNA splicing factors. During differentiation, and in a glucose-dependent manner, DDX21 displayed diminished association with nucleolar RNA accompanied by increased association with an RNA motif enriched at the junctions of differentially skipped mRNA exons. Finally, DDX21 affected the splicing of critical pro-differentiation genes independent of its helicase activity. Findings here implicating DDX21 in mRNA splicing are supported by recent work on *SMN2*.[43] Taken together, these data uncover a mechanism of glucose action as a biomolecular cue in regulating DDX21 in epidermal differentiation.

During epidermal differentiation, a general reduction in translation is observed, which would reduce energy and nutrient expenditure,[44] suggesting a non-energetic role for the increased cellular glucose concentration across differentiation. Prior work supports a role for glucose in tissue homeostasis distinct from its energetic role. For example, elevated glucose slows somatic cell proliferation and inhibits DNA and protein synthesis.[45] In skin, prolonged exposure to elevated glucose concentrations decreases the replicative life span of human epidermal keratinocytes,[45] whereas glucose is accumulated in differentiating cells in human epidermal tissue.[7] Clinically, diabetes mellitus, which characterized by elevated tissue glucose levels, is associated with poor epidermal regeneration and wound healing, although the relative contributions of elevated tissue glucose and vascular supply *in vivo* have yet to be dissected. On the other hand, an essential glucose function in epidermal differentiation has just been identified in which glucose serves as a molecular modulator of protein function,[7] supporting the role of glucose in tissue homeostasis. In this regard, metabolically stable glucose analogs readily rescue glucose restriction, and exert similar impacts on it to free glucose itself.[7]

Regulation of dimerization is a recurrently observed biological mechanism for controlling the function of diverse proteins ranging from transcription factors, to signaling proteins, to enzymes.[46] Specifically, dimerization of RBPs has been reported to increase RNA-binding affinity[47] and enzymatic activity.[27] On

Figure 6. Glucose regulates DDX21 binding to RNA introns

(A) Motif identified by HOMER *de novo* searching of DDX21 CLIP-seq peaks in differentiated keratinocytes grown in normal glucose.
(B) MST analysis of DDX21 binding to the SCUGSDGC (D: A, G, or U; S: C or G) motif RNA ("CLIP RNA"), G4 RNA or a random RNA sequence.
(C) Percentage of the indicated RNA binding to DDX21 in progenitor, differentiated cells grown in normal or low glucose in easyCLIP-seq.
(D) Percentage of DDX21 CLIP-seq reads at RNA introns in progenitor cells, differentiated cells grown in low or normal glucose.
(E) Binding of DDX21 to the *JUP* and *GRHL3* RNAs in differentiated keratinocytes grown in low (red) or normal (black) glucose. The SCUGSDGC motif and %GC are plotted as smoothed lines below in green and blue, respectively.
(F) Binding of DDX21 to the indicated RNA in progenitor, low or normal glucose in differentiated cells.
(G) Percentage of the indicated RNA binding for DDX21 WT and mutants in HEK293T cells by easyCLIP-seq.
(H) Binding of DDX21 WT and mutants to the indicated RNA in HEK293T cells.
Error bars, standard deviations from $\geq$3 biological replicates. p values, two-tailed Student's t test. FOX2 is a splicing factor control.
See also Figure S6 and Table S4.

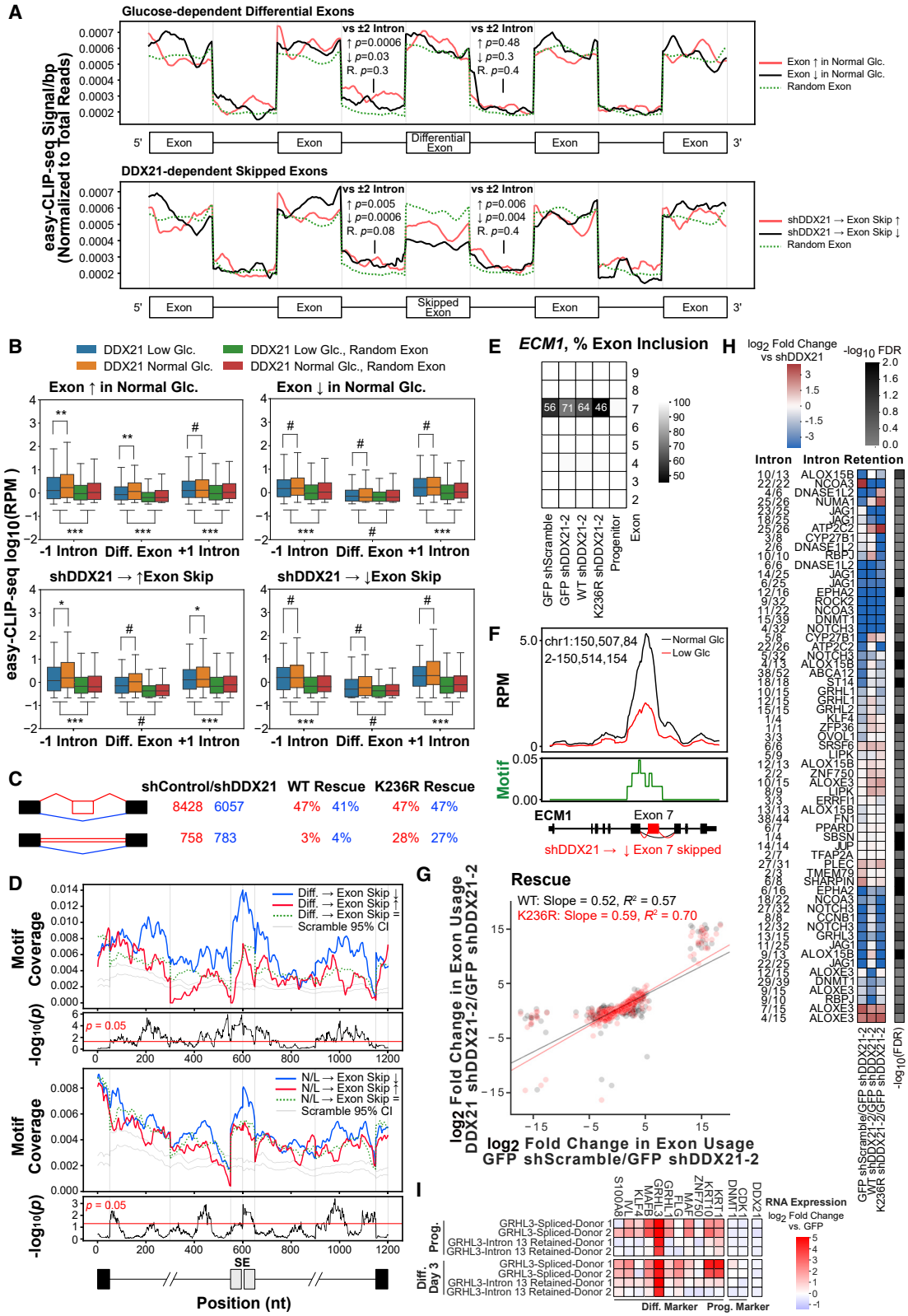

(legend on next page)

the other hand, de-dimerized RBPs may have distinct functions and locations. For example, polypyrimidine tract-binding protein (PTB) is dimeric in the nucleus and monomeric in the cytoplasm, with the cytoplasmic PTB monomer associating with ribosomes to enhance the translation of p53.[48] In this regard, 29 of 91 glucose binding proteins identified here are RBPs, with DDX21, SF3A1, G3BP1, IGF2BP3, and CCT5 among the top hits, raising the possibility that glucose may serve as a broadly acting regulator of RBP function. The present work adds to the known functions of DDX21 dimers in rRNA processing[9] to highlight the glucose-enabled role of DDX21 monomers in binding pre-mRNA to regulate nucleoplasmic mRNA processing.

CLIP-seq data here identified DDX21 binding to a specific RNA motif, SCUGSDGC, both *in vivo* and *in vitro*. SCUGSDGC-containing RNA displayed greater affinity for DDX21 than the canonical DDX21 G4 RNA sequence. It has been shown that splicing factor-dependent GC-rich exons are more dependent on U1 snRNP-associated proteins,[49] and we observed glucose-dependent DDX21 binding to U1 snRNA, suggesting DDX21's regulation of GC-rich RNA splicing could be U1 snRNA related. On the other hand, DDX21 binding to mRNA is independent of its helicase activity, and DDX21 function in pre-mRNA processing involves a non-helicase mechanism. The mechanism of DDX21 actions in this setting needs further dissection. In addition to differentiation processes studied here, both glucose[50,51] and DDX21[8,13,14] play roles in carcinogenesis. It will be of interest to determine if the dysregulation in tissue glucose levels that is seen in specific disease settings, such as cancer, affects DDX21 functions outside the context of tissue homeostasis.

Limitations of the study

The impact of glucose on RBPs was studied with respect to DDX21 and glucose's effects on the other RNA helicases and RBPs that it associates with are undefined. Additionally, potential roles for DDX21 in differentiation of non-epidermal tissues was not studied. Finally, how DDX21 regulates splicing of differentiation genes is unknown, and direct or indirect effects on splicing machinery are possible.

STAR★METHODS

Detailed methods are provided in the online version of this paper and include the following:

- KEY RESOURCES TABLE
- RESOURCE AVAILABILITY
  - Lead Contact
  - Materials availability
  - Data and code availability
- EXPERIMENTAL MODEL AND SUBJECT DETAILS
  - Cells and Organotypic Culture
- METHOD DETAILS
  - Colony Formation Assay
  - Gene Transfer and Knockdown
  - Recombinant Protein Purification
  - Microscale Thermophoresis
  - Fluorescence-based binding assay
  - Quantitative RT-PCR Expression Analysis
  - Western blot and Immunofluorescence
  - ATPase Activity Assay
  - Helicase Unwinding Assay
  - CellTiter-Blue (CTB) Cell Viability Assay
  - TUNEL Assay
  - RNA-seq
  - Nucleolus Fractionation
  - High Molecular Weight Fractionation
  - Blue Native Gel
  - Nanoscale Secondary Ion Mass Spectrometry (NanoSIMS)
  - Proximity Ligation Assay (PLA)
  - Azido-glucose Pulldown-MS
  - BioID, UVC Crosslinking and BS3 Crosslinking
  - Sample Preparation and LC-MS/MS Analysis
  - Mass Spectrometry Data Analysis
  - Homology Directed Repair Genome Editing (HDR)
  - Fast Protein Liquid Chromatography (FPLC)
  - Immunoprecipitation

Figure 7. DDX21 regulates mRNA splicing

(A and B) Traces of easyCLIP signal (A) and box plot of total signal (B) around exons differentially expressed between differentiated cells grown in low or normal glucose (top, FDR < 0.1, ≥10% difference) or around exons differentially skipped between shScramble- and shDDX21-treated cells (bottom, FDR < 0.15, ≥10% difference). The p values at ±1 introns in (A) are relative to ±2 introns.

(C) The top two forms of altered splicing upon shDDX21 loss. The number of differential events at FDR < 0.2 is given for shDDX21 knockdown, followed by the percentage of those events rescued (FDR < 0.2) by WT or K236R.

(D) Averaged coverage of the SCUGSDGC motif around exons differentially skipped upon differentiation (FDR < 0.05, top) or upon glucose restriction (FDR < 0.05, bottom). The x axis denotes the last 50 nt of the upstream exon, the first and last 250 nt of the upstream intron, the first and last 50 nt of the skipped exon. Traces are the average number of nucleotides covered by the motif in a 50 nt window excluding the first and last 2 bases of introns. Densities of 100 control motifs with nucleotide-frequency/length/degeneracy matched to the SCUGSDGC motif were calculated, and the 95% confidence interval (CI) fit independently at each point along the transcript, with the bounds of the 95% CI plotted in gray. The $\log_{10}$ p value is the enrichment of motif coverage in the 50 nt window for the blue line cases vs. non-differential exons; horizontal red line, p = 0.05.

(E) %Exon inclusion in *ECM1* mRNA. All conditions except "progenitor" are from differentiated cells. Numbers, average percentage from two biological replicates.

(F) DDX21 binding across *ECM1* mRNA in differentiated keratinocytes grown in low (red) or normal (black) glucose. Green lines, the SCUGSDGC motif (smoothed).

(G) Exon usage changes between treatment with a control shRNA vs. DDX21 loss (x axis) and rescue with WT (black) or K236R (red) DDX21 vs. DDX21 loss (y axis).

(H) Intron retention changes of progenitor and differentiation markers upon DDX21 loss or upon WT or K236R DDX21 rescue in differentiated cells.

(I) qPCR of progenitor and differentiation markers in progenitor and differentiated cells with overexpressing FHH-GFP, FHH-GRHL3, or FHH-GRHL3-intron 13-retained. Data are normalized to FHH-GFP.

Error bars, standard deviations from ≥3 biological replicates. p values, Mann-Whitney U (two-sided).

See also Figure S7 and Table S5, Table S6, and Table S7.

- CLIP-seq
- CUT&RUN-seq
- Chromatin Fractionation
- Sequencing Data Analysis

- QUANTIFICATION AND STATISTICAL ANALYSIS
  - Statistical analysis of biological data

SUPPLEMENTAL INFORMATION

Supplemental information can be found online at https://doi.org/10.1016/j.cell.2022.12.004.

ACKNOWLEDGMENTS

We thank A.E. Oro, H.Y. Chang, and J.Z. Long for pre-submission review. This work was supported by NIAMS/NIH grants AR043799 and AR045192 to P.A.K. and by a USVA Merit Review grant BX001409 to P.A.K., as well as by 1F32AR072504 to D.F.P., K01AR070895 to V.L.-P., and K01AR071481 to B.J.Z. Part of this work was performed at the Stanford Nano Shared Facilities (SNSF), supported by the National Science Foundation under award ECCS-2026822. Part of the microscope imaging was performed at Stanford University Cell Sciences Imaging Facility (CSIF) (RRID:SCR_017787). The Graphical Abstract is created with BioRender.com.

AUTHOR CONTRIBUTIONS

W.M. and P.A.K. conceived the project. W.M., D.F.P., V.L.-P., R.M.M., I.D.F., J.M.M., A.W.H., and D.L.R. performed experiments. Z.S., D.T.N., and L.A.K. edited genes by HDR. W.M., Y.B., M.M.M., C.E.J.-R., and C.-G.W. performed NanoSIMS experiment. Y.-Y.Y. and Y.W. performed MS analysis. D.F.P. analyzed sequencing data. W.M., I.D.F., and M.R. analyzed MS data. B.J.Z., S.J., G.P.N., and R.A.F. provided helpful discussions and methodology. S.T. cultured all the primary cells. V.L.-P. and P.A.K. guided experiments and data analysis. W.M., D.F.P., V.L.-P., Z.S., and P.A.K. wrote the manuscript.

DECLARATION OF INTERESTS

The authors declare no competing interests.

Received: April 11, 2022
Revised: October 17, 2022
Accepted: December 2, 2022
Published: January 5, 2023

REFERENCES

1. Lopez-Pajares, V., Yan, K., Zarnegar, B.J., Jameson, K.L., and Khavari, P.A. (2013). Genetic pathways in disorders of epidermal differentiation. Trends Genet. *29*, 31–40.
2. Bikle, D.D., Xie, Z., and Tu, C.-L. (2012). Calcium regulation of keratinocyte differentiation. Expert Rev. Endocrinol. Metab. *7*, 461–472.
3. Fuchs, E. (2007). Scratching the surface of skin development. Nature *445*, 834–842.
4. Moreci, R.S., and Lechler, T. (2020). Epidermal structure and differentiation. Curr. Biol. *30*, R144–R149.
5. Hay, R.J., Johns, N.E., Williams, H.C., Bolliger, I.W., Dellavalle, R.P., Margolis, D.J., Marks, R., Naldi, L., Weinstock, M.A., Wulf, S.K., et al. (2014). The global burden of skin disease in 2010: an analysis of the prevalence and impact of skin conditions. J. Invest. Dermatol. *134*, 1527–1534.
6. Kim, D.S., Risca, V.I., Reynolds, D.L., Chappell, J., Rubin, A.J., Jung, N., Donohue, L.K.H., Lopez-Pajares, V., Kathiria, A., Shi, M., et al. (2021). The dynamic, combinatorial cis-regulatory lexicon of epidermal differentiation. Nat. Genet. *53*, 1564–1576.
7. Lopez-Pajares, V., Bhaduri, A., Zhao, Y., Gowrishankar, G., Donohue, L., Guo, M.G., Siprashvilli, Z., Miao, W., Nguyen, D.T., Li, A., et al. (2022). Glucose modulates transcription factor dimerization to enable tissue differentiation https://doi.org/10.1101/2022.11.28.518222.
8. Song, C., Hotz-Wagenblatt, A., Voit, R., and Grummt, I. (2017). SIRT7 and the DEAD-box helicase DDX21 cooperate to resolve genomic R loops and safeguard genome stability. Genes Dev. *31*, 1370–1381.
9. Calo, E., Flynn, R.A., Martin, L., Spitale, R.C., Chang, H.Y., and Wysocka, J. (2015). RNA helicase DDX21 coordinates transcription and ribosomal RNA processing. Nature *518*, 249–253.
10. Xing, Y.-H., Yao, R.-W., Zhang, Y., Guo, C.-J., Jiang, S., Xu, G., Dong, R., Yang, L., and Chen, L.L. (2017). SLERT regulates DDX21 rings associated with Pol I transcription. Cell *169*, 664–678.e16.
11. Westermarck, J., Weiss, C., Saffrich, R., Kast, J., Musti, A.-M., Wessely, M., Ansorge, W., Seraphin, B., Wilm, M., Valdez, B.C., and Bohmann, D. (2002). The DEXD/H-box RNA helicase RHII/Gu is a co-factor for c-Jun-activated transcription. EMBO J. *21*, 451–460.
12. Zhang, Y., Baysac, K.C., Yee, L.-F., Saporita, A.J., and Weber, J.D. (2014). Elevated DDX21 regulates c-Jun activity and rRNA processing in human breast cancers. Breast Cancer Res. *16*, 449.
13. Cao, J., Wu, N., Han, Y., Hou, Q., Zhao, Y., Pan, Y., Xie, X., and Chen, F. (2018). DDX21 promotes gastric cancer proliferation by regulating cell cycle. Biochem. Biophys. Res. Commun. *505*, 1189–1194.
14. Santoriello, C., Sporrij, A., Yang, S., Flynn, R.A., Henriques, T., Dorjsuren, B., Custo Greig, E., McCall, W., Stanhope, M.E., Fazio, M., et al. (2020). RNA helicase DDX21 mediates nucleotide stress responses in neural crest and melanoma cells. Nat. Cell Biol. *22*, 372–379.
15. Johansson, J.A., Marie, K.L., Lu, Y., Brombin, A., Santoriello, C., Zeng, Z., Zich, J., Gautier, P., von Kriegsheim, A., Brundson, H., et al. (2020). PRL3-DDX21 transcriptional control of endolysosomal genes restricts melanocyte stem cell differentiation. Dev. Cell *54*, 317–332.e9.
16. Jankowsky, E., and Fairman, M.E. (2007). RNA helicases — one fold for many functions. Curr. Opin. Struct. Biol. *17*, 316–324.
17. Tsherniak, A., Vazquez, F., Montgomery, P.G., Weir, B.A., Kryukov, G., Cowley, G.S., Gill, S., Harrington, W.F., Pantel, S., Krill-Burger, J.M., et al. (2017). Defining a cancer dependency map. Cell *170*, 564–576.e16.
18. Rubin, A.J., Parker, K.R., Satpathy, A.T., Qi, Y., Wu, B., Ong, A.J., Mumbach, M.R., Ji, A.L., Kim, D.S., Cho, S.W., et al. (2019). Coupled single-cell CRISPR screening and epigenomic profiling reveals causal gene regulatory networks. Cell *176*, 361–376.e17.
19. Kretz, M., Siprashvili, Z., Chu, C., Webster, D.E., Zehnder, A., Qu, K., Lee, C.S., Flockhart, R.J., Groff, A.F., Chow, J., et al. (2013). Control of somatic tissue differentiation by the long non-coding RNA TINCR. Nature *493*, 231–235.
20. Jameson, K.L., Mazur, P.K., Zehnder, A.M., Zhang, J., Zarnegar, B., Sage, J., and Khavari, P.A. (2013). IQGAP1 scaffold-kinase interaction blockade selectively targets RAS-MAP kinase–driven tumors. Nat. Med. *19*, 626–630.
21. Chen, H., Ahsan, S.S., Santiago-Berrios, M.E.B., Abruña, H.D., and Webb, W.W. (2010). Mechanisms of quenching of Alexa fluorophores by natural amino acids. J. Am. Chem. Soc. *132*, 7244–7245.
22. Kozlov, A.G., Galletto, R., and Lohman, T.M. (2012). SSB-DNA binding monitored by fluorescence intensity and anisotropy. Methods Mol. Biol. *922*, 55–83.
23. Chen, Z., Li, Z., Hu, X., Xie, F., Kuang, S., Zhan, B., Gao, W., Chen, X., Gao, S., Li, Y., et al. (2020). Structural basis of human helicase DDX21 in RNA binding, unwinding, and antiviral signal activation. Adv. Sci. (Weinh) *7*, 2000532.
24. Trott, O., and Olson, A.J. (2010). AutoDock Vina: improving the speed and accuracy of docking with a new scoring function, efficient optimization, and multithreading. J. Comput. Chem. *31*, 455–461.
25. Pettersen, E.F., Goddard, T.D., Huang, C.C., Couch, G.S., Greenblatt, D.M., Meng, E.C., and Ferrin, T.E. (2004). UCSF Chimera—A visualization

system for exploratory research and analysis. J. Comput. Chem. *25*, 1605–1612.

26. Lee, H.S., Jo, S., Lim, H.-S., and Im, W. (2012). Application of binding free energy calculations to prediction of binding modes and affinities of MDM2 and MDMX inhibitors. J. Chem. Inf. Model. *52*, 1821–1832.
27. Marcaida, M.J., Kauzlaric, A., Duperrex, A., Sülzle, J., Moncrieffe, M.C., Adebajo, D., Manley, S., Trono, D., and Dal Peraro, M. (2020). The human RNA helicase DDX21 presents a dimerization interface necessary for helicase activity. iScience *23*, 101811.
28. Hirai, Y., Louvet, E., Oda, T., Kumeta, M., Watanabe, Y., Horigome, T., and Takeyasu, K. (2013). Nucleolar scaffold protein, WDR46, determines the granular compartmental localization of nucleolin and DDX21. Genes Cells *18*, 780–797.
29. Skene, P.J., and Henikoff, S. (2017). An efficient targeted nuclease strategy for high-resolution mapping of DNA binding sites. eLife *6*, e21856.
30. Damianov, A., Ying, Y., Lin, C.-H., Lee, J.-A., Tran, D., Vashisht, A.A., Bahrami-Samani, E., Xing, Y., Martin, K.C., Wohlschlegel, J.A., and Black, D.L. (2016). Rbfox proteins regulate splicing as part of a large multiprotein complex LASR. Cell *165*, 606–619.
31. Roux, K.J., Kim, D.I., Burke, B., and May, D.G. (2018). BioID: A screen for protein-protein interactions. Curr. Protoc. Protein Sci. *91*, 19.23.1–19.23.15.
32. Ramanathan, M., Majzoub, K., Rao, D.S., Neela, P.H., Zarnegar, B.J., Mondal, S., Roth, J.G., Gai, H., Kovalski, J.R., Siprashvili, Z., et al. (2018). RNA–protein interaction detection in living cells. Nat. Methods *15*, 207–212.
33. Porter, D.F., Miao, W., Yang, X., Goda, G.A., Ji, A.L., Donohue, L.K.H., Aleman, M.M., Dominguez, D., and Khavari, P.A. (2021). easyCLIP analysis of RNA-protein interactions incorporating absolute quantification. Nat. Commun. *12*, 1569.
34. McRae, E.K.S., Booy, E.P., Moya-Torres, A., Ezzati, P., Stetefeld, J., and McKenna, S.A. (2017). Human DDX21 binds and unwinds RNA guanine quadruplexes. Nucleic Acids Res. *45*, 6656–6668.
35. Ren, X., Zhang, K., Deng, R., and Li, J. (2019). RNA splicing analysis: from in vitro testing to single-cell imaging. Chem *5*, 2571–2592.
36. Shen, S., Park, J.W., Lu, Z.-x., Lin, L., Henry, M.D., Wu, Y.N., Zhou, Q., and Xing, Y. (2014). rMATS: robust and flexible detection of differential alternative splicing from replicate RNA-Seq data. Proc. Natl. Acad. Sci. USA *111*, E5593–E5601.
37. Smits, P., Poumay, Y., Karperien, M., Tylzanowski, P., Wauters, J., Huylebroeck, D., Ponec, M., and Merregaert, J. (2000). Differentiation-dependent alternative splicing and expression of the extracellular matrix Protein 1 gene in human keratinocytes. J. Invest. Dermatol. *114*, 718–724.
38. Hamada, T., McLean, W.H.I., Ramsay, M., Ashton, G.H.S., Nanda, A., Jenkins, T., Edelstein, I., South, A.P., Bleck, O., Wessagowit, V., et al. (2002). Lipoid proteinosis maps to 1q21 and is caused by mutations in the extracellular matrix protein 1 gene (ECM1). Hum. Mol. Genet. *11*, 833–840.
39. Chan, I. (2004). The role of extracellular matrix protein 1 in human skin. Clin. Exp. Dermatol. *29*, 52–56.
40. Ting, S.B., Caddy, J., Hislop, N., Wilanowski, T., Auden, A., Zhao, L.L., Ellis, S., Kaur, P., Uchida, Y., Hollerman, W.M., et al. (2005). A Homolog of Drosophila grainy head Is Essential for Epidermal Integrity in Mice. Science *308*, 411–413.
41. Wilanowski, T., Caddy, J., Ting, S.B., Hislop, N.R., Cerruti, L., Auden, A., Zhao, L.L., Asquith, S., Ellis, S., Sinclair, R., et al. (2008). Perturbed desmosomal cadherin expression in grainy head-like 1-null mice. EMBO J. *27*, 886–897.
42. Mlacki, M., Darido, C., Jane, S.M., and Wilanowski, T. (2014). Loss of Grainy head-like 1 is associated with disruption of the epidermal barrier and squamous cell carcinoma of the skin. PloS one *9*, e89247.
43. Gong, M., Zhang, X., Wang, Y., Mao, G., Ou, Y., Wei, C., Hu, X., and Xiang, S. (2021). DDX21 interacts with nuclear AGO2 and regulates the alternative splicing of SMN2. Biosci. Biotechnol. Biochem. *85*, 272–279.
44. Collier, A.E., Wek, R.C., and Spandau, D.F. (2017). Human keratinocyte differentiation requires translational control by the eIF2α kinase GCN2. J. Invest. Dermatol. *137*, 1924–1934.
45. Terashi, H., Izumi, K., Deveci, M., Rhodes, L.M., and Marcelo, C.L. (2005). High glucose inhibits human epidermal keratinocyte proliferation for cellular studies on diabetes mellitus. Int. Wound J. *2*, 298–304.
46. Marianayagam, N.J., Sunde, M., and Matthews, J.M. (2004). The power of two: protein dimerization in biology. Trends Biochem. Sci. *29*, 618–625.
47. Ripin, N., Boudet, J., Duszczyk, M.M., Hinniger, A., Faller, M., Krepl, M., Gadi, A., Schneider, R.J., Sponer, J., Meisner-Kober, N.C., et al. (2019). Molecular basis for AU-rich element recognition and dimerization by the HuR C-terminal RRM. Proc. Natl. Acad. Sci. USA *116*, 2935–2944.
48. Gong, F.-X., Zhan, G., Han, R., Yang, Z., Fu, X., and Xiao, R. (2021). Dedimerization of PTB is catalyzed by PDI and is involved in the regulation of p53 translation. Nucleic Acids Res. *49*, 9342–9352.
49. Lemaire, S., Fontrodona, N., Aubé, F., Claude, J.-B., Polvèche, H., Modolo, L., Bourgeois, C.F., Mortreux, F., and Auboeuf, D. (2019). Characterizing the interplay between gene nucleotide composition bias and splicing. Genome Biol. *20*, 259.
50. Adekola, K., Rosen, S.T., and Shanmugam, M. (2012). Glucose transporters in cancer metabolism. Curr. Opin. Oncol. *24*, 650–654.
51. Lin, X., Xiao, Z., Chen, T., Liang, S.H., and Guo, H. (2020). Glucose metabolism on tumor plasticity, diagnosis, and treatment. Front. Oncol. *10*, 317.
52. Perez-Riverol, Y., Csordas, A., Bai, J., Bernal-Llinares, M., Hewapathirana, S., Kundu, D.J., Inuganti, A., Griss, J., Mayer, G., Eisenacher, M., et al. (2019). The PRIDE database and related tools and resources in 2019: improving support for quantification data. Nucleic Acids Res. *47*, D442–D450.
53. Truong, A.B., Kretz, M., Ridky, T.W., Kimmel, R., and Khavari, P.A. (2006). p63 regulates proliferation and differentiation of developmentally mature keratinocytes. Genes Dev. *20*, 3185–3197.
54. Shave, S., Chen, Y.-K., Pham, N.T., and Auer, M. (2021). PyBindingCurve, simulation, and curve fitting to complex binding systems at equilibrium. J. Chem. Inf. Model. *61*, 2911–2915.
55. Özeş, A.R., Feoktistova, K., Avanzino, B.C., Baldwin, E.P., and Fraser, C.S. (2014). Real-time fluorescence assays to monitor duplex unwinding and ATPase activities of helicases. Nat. Protoc. *9*, 1645–1661.
56. Mellacheruvu, D., Wright, Z., Couzens, A.L., Lambert, J.-P., St-Denis, N.A., Li, T., Miteva, Y.V., Hauri, S., Sardiu, M.E., Low, T.Y., et al. (2013). The CRAPome: a contaminant repository for affinity purification–mass spectrometry data. Nat. Methods *10*, 730–736.
57. Schmidt, C., and Robinson, C.V. (2014). A comparative cross-linking strategy to probe conformational changes in protein complexes. Nat. Protoc. *9*, 2224–2236.
58. Cox, J., and Mann, M. (2008). MaxQuant enables high peptide identification rates, individualized p.p.b.-range mass accuracies and proteome-wide protein quantification. Nat. Biotechnol. *26*, 1367–1372.
59. Mendes, M.L., Fischer, L., Chen, Z.A., Barbon, M., O'Reilly, F.J., Giese, S.H., Bohlke-Schneider, M., Belsom, A., Dau, T., Combe, C.W., et al. (2019). An integrated workflow for crosslinking mass spectrometry. Mol. Syst. Biol. *15*, e8994.
60. Fischer, L., and Rappsilber, J. (2017). Quirks of error estimation in cross-linking/mass spectrometry. Anal. Chem. *89*, 3829–3833.
61. Labun, K., Montague, T.G., Krause, M., Torres Cleuren, Y.N., Tjeldnes, H., and Valen, E. (2019). CHOPCHOP v3: expanding the CRISPR web toolbox beyond genome editing. Nucleic Acids Res. *47*, W171–W174.
62. Porter, D.F., Garg, R.M., Meyers, R.M., Miao, W., Ducoli, L., Zarnegar, B.J., and Khavari, P.A. (2021). Modified forms of easyCLIP https://doi.org/10.1101/2021.12.15.472862.
63. Liu, N., Hargreaves, V.V., Zhu, Q., Kurland, J.V., Hong, J., Kim, W., Sher, F., Macias-Trevino, C., Rogers, J.M., Kurita, R., et al. (2018). Direct

promoter repression by BCL11A controls the fetal to adult hemoglobin switch. Cell *173*, 430–442.e17.

64. Li, L., Miao, W., Huang, M., Williams, P., and Wang, Y. (2019). Integrated genomic and proteomic analyses reveal novel mechanisms of the methyltransferase SETD2 in renal cell carcinoma development. Mol. Cell. Proteomics *18*, 437–447.
65. Martin, M. (2011). Cutadapt removes adapter sequences from high-throughput sequencing reads. EMBnet. j. *17*, 10–12.
66. Langmead, B., and Salzberg, S.L. (2012). Fast gapped-read alignment with Bowtie 2. Nat. Methods *9*, 357–359.
67. Gaspar, J.M. (2018). Improved peak-calling with MACS2 https://doi.org/10.1101/496521.
68. Zhang, Y., Liu, T., Meyer, C.A., Eeckhoute, J., Johnson, D.S., Bernstein, B.E., Nusbaum, C., Myers, R.M., Brown, M., Li, W., and Liu, X.S. (2008). Model-based analysis of ChIP-seq (MACS). Genome Biol. *9*, R137.
69. Quinlan, A.R., and Hall, I.M. (2010). BEDTools: a flexible suite of utilities for comparing genomic features. Bioinformatics Oxf. Engl. *26*, 841–842.
70. Dobin, A., Davis, C.A., Schlesinger, F., Drenkow, J., Zaleski, C., Jha, S., Batut, P., Chaisson, M., and Gingras, T.R. (2013). STAR: ultrafast universal RNA-seq aligner. Bioinformatics *29*, 15–21.
71. Li, B., and Dewey, C.N. (2011). RSEM: accurate transcript quantification from RNA-Seq data with or without a reference genome. BMC Bioinformatics *12*, 323.
72. Soneson, C., Matthes, K.L., Nowicka, M., Law, C.W., and Robinson, M.D. (2016). Isoform prefiltering improves performance of count-based methods for analysis of differential transcript usage. Genome Biol. *17*, 12.
73. Liao, Y., Smyth, G.K., and Shi, W. (2019). The R package Rsubread is easier, faster, cheaper and better for alignment and quantification of RNA sequencing reads. Nucleic Acids Res. *47*, e47.
74. Anders, S., Reyes, A., and Huber, W. (2012). Detecting differential usage of exons from RNA-seq data. Genome Res. *22*, 2008–2017.
75. Middleton, R., Gao, D., Thomas, A., Singh, B., Au, A., Wong, J.J.L., Bomane, A., Cosson, B., Eyras, E., Rasko, J.E., and Ritchie, W. (2017). IRFinder: assessing the impact of intron retention on mammalian gene expression. Genome Biol. *18*, 51.
76. Audic, S., and Claverie, J.M. (1997). The significance of digital gene expression profiles. Genome Res. *7*, 986–995.
77. Storer, J., Hubley, R., Rosen, J., Wheeler, T.J., and Smit, A.F. (2021). The Dfam community resource of transposable element families, sequence models, and genome annotations. Mobile DNA *12*, 2.
78. Chen, E.Y., Tan, C.M., Kou, Y., Duan, Q., Wang, Z., Meirelles, G.V., Clark, N.R., and Ma'ayan, A. (2013). Enrichr: interactive and collaborative HTML5 gene list enrichment analysis tool. BMC Bioinformatics *14*, 128.
79. Kuleshov, M.V., Jones, M.R., Rouillard, A.D., Fernandez, N.F., Duan, Q., Wang, Z., Koplev, S., Jenkins, S.L., Jagodnik, K.M., Lachmann, A., et al. (2016). Enrichr: a comprehensive gene set enrichment analysis web server 2016 update. Nucleic Acids Res. *44*, W90–W97.
80. Xie, Z., Bailey, A., Kuleshov, M.V., Clarke, D.J.B., Evangelista, J.E., Jenkins, S.L., Lachmann, A., Wojciechowicz, M.L., Kropiwnicki, E., Jagodnik, K.M., et al. (2021). Gene set knowledge discovery with Enrichr. Curr. Protoc. *1*, e90.

STAR★METHODS

KEY RESOURCES TABLE

REAGENT or RESOURCE	SOURCE	IDENTIFIER
Antibodies		
anti-DDX21	ProteinTech	10528-1-AP; RRID:AB_2092705
anti-DDX21	Novus Biologicals	BP1-83310; RRID:AB_11027665
anti-H3K27me3	Active Motif	39055; RRID:AB_2561020
anti-HA	Abcam	ab130275; RRID:AB_11156884
anti-HA	CST	#3724; RRID:AB_1549585
anti-HA	ThermoFisher	#26183; RRID:AB_10978021
anti-V5	CST	#13202; RRID:AB_2687461
anti-HNRNPUL1	MyBioSource	MBS2524350
anti-HNRNPC	Santa Cruz Biotechnology	sc-32308; RRID:AB_627731
anti-HNRNPF/H	Santa Cruz Biotechnology	sc-32310; RRID:AB_2248257
anti-Actin	Millipore Sigma	A2228; RRID:AB_476697
anti-HNRNPA2B1	Santa Cruz Biotechnology	sc-374053; RRID:AB_10947257
anti-H3	CST	#14269; RRID:AB_2756816
anti-Fibrillarin	CST	#2639; RRID:AB_2278087
anti-Tubulin	Millipore Sigma	T9026; RRID:AB_477593
anti-Strept	LI-COR	926-32230
anti-KRT1	Covance	PRB-149P; RRID:AB_291572
anti-KRT10	Neomarkers	MS611P; RRID:AB_142592
anti-Ki67	Neomarkers	SP6
anti-CollagenVII	Chemicon	MAB1345; RRID:AB_94355
anti-CollagenVII	Chemicon	234192; RRID:AB_211739
Cell Lines		
Lenti-X 293T	Takara Bio	#632180
Human primary normal skin cells	Stanford University School of Medicine	GDS
Reagents and Materials		
Stellar Competent Cells	Takara Bio	#636763
DMEM	Gibco	#11995-065
Keratinocyte-SFM	Gibco	#17005-142
Medium 154	Gibco	#M-154-500
Medium 154CF	Gibco	#M-154CF-500
DMEM, no glucose	Gibco	#11966025
rEGF	Gibco	#10450-013
BPE	Gibco	13028-014
Sodium Pyruvate	Gibco	11360070
200 g/L glucose	Gibco	A2494001
Lipofectamine 3000	Invitrogen	L3000015
Lenti-X concentrator	Takara Bio	631231
Protease Inhibitor Cocktail	Sigma	P8340
anti-FLAG M2 affinity gel	Millipore Sigma	A2220
InstantBlue Coomassie Protein Stain	Abcam	ab119211
Monolith His-Tag Labeling Kit RED-tris-NTA	Nanotemper Technologies	MO-L018
Amicon columns	Millipore	UFC500396
Monolith NT.115 Capillaries	NanoTemper Technologies	MO-K022

(*Continued on next page*)

Continued

REAGENT or RESOURCE	SOURCE	IDENTIFIER
Monolith NT.115 Premium Capillaries	NanoTemper Technologies	MO-K025
Galactose	Sigma	G6404
Glucose	Sigma	49139
3-O-methyl-D-glucopyranose	Sigma	M4879
10 mM ATP	Promega	V915A
AZDye 488 Alkyne	Click ChemTools	1277-1
2-Azido-2-deoxy-D-glucose	Santa Cruz Biotechnology	sc-256068
RNeasy Plus Kit	QIAGEN	74136
iScript cDNA Synthesis Kit	Bio-Rad	1708891
SYBR Green Master Mix	Thermo Fishier	K0223
Bradford assay	Bio-Rad	5000201
16% paraformaldehyde	Alfa Aesar	43368
16% formaldehyde	Pierce	28906
Nucleolus Bright Red	Dojindo	N512-10
ADP-Glo kinase assay kit	Promega	V6930
CellTiter Blue Cell Viability Assay	Promega	G8080
RiboLock RNase Inhibitor	Thermo Fishier	EO0381
In Situ Cell Death Detection Kit, TMR red	Sigma	12156792910
QuantSeq 3′ mRNA-Seq Library Prep Kit FWD for Illumina	Lexogen	015.96
NEB Ultra II (non-directional) kit	NEB	E6111
NativePAGE™ 4 to 16%, Bis-Tris gels	Invitrogen	BN1004BOX
G-250 Sample Additive	Invitrogen	BN2004
4X Sample Buffer	Invitrogen	BN2003
Silver Stain kit	Pierce	#24612
Click-&-Go Click Chemistry Capture Kit	Click Chemistry Tools	#1065
MagReSyn Streptavidin beads	Resyn Biosciences	MR-STV010
BS3 (bis(sulfosuccinimidyl)suberate)	ThermoFisher	#21580
LDS sample loading buffer	Invitrogen	NP0008
Trypsin/Lys-C	Promega	V5071
Iodoacetamide	Sigma	I1149-5G
Dithiothreitol	MP Biomedicals	856126
OMIX C18 pipet tips	Agilent Technologies	A57003100
Superose 6 Increase 10/300 column	Cytiva	29-0915-96
Gel Filtration Standards	BioRad	#1511901
IgG	CST	#2729
Protein G dynabeads	Invitrogen	10004D
Ambion RNAse I	ThermoFisher	#AM2294
AMPure XP beads	Beckman	#A63880
Human Keratinocyte Nucleofector™ Kit	Lonza	VPD-1002
Qiagen gel extraction kit	Qiagen	#28706X4
4% agarose E-Gel with SYBR Safe DNA Gel Stain	ThermoFisher	A42136
anti-HA magnetic beads	ThermoFisher	#88837
RNaseA	Qiagen	1032724
PCR purification kit	Qiagen	28106
Qubit High Sensitivity dsDNA kit	Invitrogen	Q32851
Benzonase	Sigma	E1014-25KU
VECTABOND® Reagent	Vector Laboratories	SP-1800-7
D_4 ATP	Cambrige Isotope Lab	DLM-8922-CA-20
$^{13}C_6$ glucose	Sigma	#389374
CUTANA™ ChIC/CUT&RUN Kit	EpiCypher	14-1048

(*Continued on next page*)

Continued

REAGENT or RESOURCE	SOURCE	IDENTIFIER
Concanavalin A beads	EpiCypher	21-1401
pAG-MNase	EpiCypher	15-1016
Zymo DNA Clean and Concentrator	Zymo Research	D4014
NEBNext Ultra II DNA library prep kit	NEB	E7103S
Duolink® In Situ Orange Starter Kit Mouse/Rabbit	Sigma	DUO92102-1KT
Duolink® In Situ Mounting Medium with DAPI	Sigma	DUO82040-5ML
Plasmids		
pLKO.1-blasti	Addgene	#26655
pLKO.1-puro	Addgene	#10878
pLEX-FHH-Empty Vector-IRES-Puro	Addgene	#120568
pAAV-SEPT-Acceptor	Addgene	#25648
pBluescript II KS (+)	Addgene	#212207
pLEX-HA-BASU-Puro	In this paper	N/A
pLEX-FHH-DDX21-WT	In this paper	N/A
pLEX-FHH-DDX21-WT-Mut for shD2	In this paper	N/A
pLEX-FHH-DDX21-K236R	In this paper	N/A
pLEX-FHH-DDX21-K236R-Mut for shD2	In this paper	N/A
pLEX-FHH-DDX21-K236G	In this paper	N/A
pLEX-FHH-DDX21-K236G-Mut for shD2	In this paper	N/A
pLEX-FHH-DDX21-611R	In this paper	N/A
pLEX-FHH-DDX21-611R-Mut for shD2	In this paper	N/A
pLEX-FHH-DDX21-611Del	In this paper	N/A
pLEX-FHH-DDX21-V276W	In this paper	N/A
pLEX-FHH-DDX21-V276W-Mut for shD2	In this paper	N/A
pLEX-FHH-GFP	In this paper	N/A
pLEX-FHH-GRHL3-Spliced	In this paper	N/A
pLEX-FHH-GRHL3-Intron 13 Retained	In this paper	N/A
pLEX-FH-DDX21-WT	In this paper	N/A
pLEX-HA-BASU-DDX21-WT	In this paper	N/A
pLEX-HA-BASU-DDX21-K236R	In this paper	N/A
pLEX-uORF-HA-BASU-NLS-GFP	In this paper	N/A
pLEX-HA-BASU-NLS-GFP	In this paper	N/A
pLEX-V5-DDX21-WT	In this paper	N/A
pLEX-V5-HNRNPUL1	In this paper	N/A
pLEX-V5-HNRNPA2B1	In this paper	N/A
pLKO.1-puro-shScramble	In this paper	N/A
pLKO.1-puro-shDDX21-1	In this paper	N/A
pLKO.1-puro-shDDX21-2	In this paper	N/A
pLKO.1-puro-shDDX21-3	In this paper	N/A
pLKO.1-blasti-shScramble	In this paper	N/A
pLKO.1-blasti-shDDX21-2	In this paper	N/A
pAAV-K236	In this paper	N/A
pAAV-L611	In this paper	N/A

RESOURCE AVAILABILITY

Lead Contact

Further information and requests for resources and reagents should be directed to and will be fulfilled by the lead contact, Paul A. Khavari (khavari@stanford.edu).

Materials availability

All unique/stable reagents generated in this study are available from the lead contact without restriction.

Data and code availability

All the mass spectrometry raw files have been deposited to the ProteomeXchange Consortium via the PRIDE[52] partner repository with the dataset identifier PXD028561. All the sequencing data files are available from GEO, accession GSE189914. All the code has been deposited at Zenodo with DOI of 10.5281/zenodo.7275312. Any additional information required to reanalyze the data reported in this paper is available from the lead contact upon request.

EXPERIMENTAL MODEL AND SUBJECT DETAILS

Cells and Organotypic Culture

HEK293T (Takara Bio, #632180) cells were maintained in Dulbecco's modified Eagle's medium (DMEM) media (Gibco, #11995-065) supplemented with 10% fetal bovine serum (FBS) and 1% penicillin–streptomycin at 37°C with 5% CO_2. Primary human keratinocytes were isolated from fresh surgically discarded newborn foreskin, and progenitor cells were cultured in 50% (v:v) complete Keratinocyte-SFM (Gibco, #17005-142) and 50% (v:v) Medium 154 (Gibco, #M-154-500). Cells were induced to differentiate by the addition of 1.2 mM calcium for 3 days at full confluence in the 50/50 media if not notified specifically. Cells with low glucose and the corresponding normal glucose condition were maintained in glucose-free DMEM (Gibco, #11966025) supplied with SFM supplement (rEGF: Gibco, #10450-013; BPE: 13028-014), 1X Sodium Pyruvate (Gibco, 11360070) and a final concentration of 0.5 g/L ("low" glucose, Gibco, A2494001) or 4.5 g/L glucose ("normal" glucose) with adding 1.2 mM calcium during differentiation for 3 days. All the "low" and "normal" conditions indicated referred to day 3 differentiated cells if not specified. All the progenitor cells were maintained in 50/50 media if not specified. Organotypic regeneration of human epidermal tissue were performed as previously described[53] using KGM media if not notified specifically. Day 7 epidermal tissues were collected. Biological replicates were performed in all cases using primary cells from at least 2 independent, unrelated donors. Cells were tested regularly for Mycoplasma contamination; none tested positive throughout the studies.

METHOD DETAILS

Colony Formation Assay

Cells were seeded in six-well plates at a density of 150 cells/well. Cells were maintained in complete Keratinocyte-SFM and Medium 154 for 7 days to form colonies and in "low" or "normal" glucose DMEM for another 4 days. At day 11, the cells were washed once with phosphate-buffered saline (PBS), fixed with 70% ethanol for 10 min, stained with 0.2% crystal violet for 10 min, and subsequently washed with water five times. Colonies and their size were determined by ImageJ and counted using ImageJ.

Gene Transfer and Knockdown

To produce viruses, HEK293T cells in 10 cm plates were transfected with 9 μg of each retroviral expression construct, using Lipofectamine 3000 (Invitrogen, L3000015). Viral supernatants were collected 48 hours after transfection and concentrated using Lenti-X concentrator (TaKaRa, 631231). For infection, the optimized viral titer was added to primary human keratinocytes and HEK293T cells together with polybrene (5 μg/mL). The next day, fresh media was added, and cells were selected using puromycin (1 μg/mL) or blasticidin (5 μg/mL). The sequence of the retained intron 13 added to GRHL3 gene is gggacctcccgccctcctcatttactcaccaggcccacccc agctcccacctccctcatgggctttcccaaagcctccttggggtggggcacgaggcgctgccttacccctggagctaggtttaggttaagacttgggggtgggggtaaggaggga acctcaggctgcttggagagaccaccacaggactggcggcttctgtctcctgacctcgtgtggacgtgggagtcctgggcagctggcatagtcagcaggctgattatgctgggcga gtccccctctcccacttttctgatggggagtgggagaagggtggggttttgatgtctggctttcttgctttgaccctctaaatctgttacttccttggggtggggaacaagcccaaacct ctgggggctgtagctggccatcaggaagaaaccaactagcagctaagctcaaaagcttccagcagccatgaatcgagctttgcgtggcacctcgtgtttccagacactgccatcaa ttcccacaatgactctacgaaacagcggacagagcctccattttacatgcaaataaaatcaggctccgtgatgttaaaatcacgtttgcaaggtcacctggctggcaggtagtagagc aggggttcagacacccccacataagcacagcttaagagggtgcatgggaatctgcagagccggccaaagggcctcccagctgggcaaagacccgcagcagaagtcaatcttc aagtaacgttttcagattccccagcccctgagatgatcctgttcacattatcttccttgcactcaagctggcccttgcttttcaa with double splice mutated. shRNAs targeting DDX21 were designed based on Sigma sequences (https://www.sigmaaldrich.com/US/en/semi-configurators/shrna?activeLink=productSearch) and were cloned into pLKO.1-puro or pLKO.1-blasti plasmid (Addgene, #10878 and #26655). The targeting sequences are listed below.

shScramble, 5'-TCCTAAGGTTAAGTCGCCCTCG-3';
shDDX21-1, 5'-CCTGAGGTTGATTTGGTTATA-3';
shDDX21-2, 5'-GCATGAGGAATGGGATTGATA-3';
shDDX21-3, 5'-CCCATATCTGAAGAAACTATT-3'.

Recombinant Protein Purification

All recombinant target proteins were produced in HEK293T cells. Briefly, 20 μg of pLEX FHH- or pLEX FH- tagged target protein plasmid was transfected per 15 cm plate of ~80% confluent HEK293T cells, using Lipofectamine 3000 (Invitrogen). 48 hours after transfection, cells were harvested, lysed on ice for 30 minutes in lysis buffer (50 mM Tris-HCl pH 7.5, 300 mM NaCl, 1 mM EDTA, 1% Triton X-100, 1X Protease Inhibitor Cocktail [Sigma, P8340]), then sonicated for 3 cycles of 10 seconds at an amplitude of 10% followed by a 10 second pause. The lysate was centrifuged at 16,000 g for 10 minutes and quantified. The lysate was added to a saturating volume of anti-FLAG M2 affinity gel (Millipore Sigma, A2220) – a volume determined by a small scale, pilot purification for each protein. The IP was performed overnight at 4°C and the next morning was washed three times with wash buffer (50 mM Tris-HCl pH 7.5, 3 mM EDTA, 0.5% NP-40, 500 mM NaCl, 10% Glycerol, 0.1 mM DTT). Before elution, M2 beads were primed with two washes of Elution Buffer (1X PBS), then purified protein was eluted using 0.5 mg/mL 3X FLAG peptide in Elution Buffer. Elution was performed once at 1.5X bead volume for 1 hour. Eluates were concentrated using 3k molecular weight cutoff Amicon columns (Millipore, UFC500396). Finally, the target protein concentration was determined by running purified protein and a BSA standard curve on a Bis-Tris gel and staining using InstantBlue Coomassie Protein Stain (Abcam, ab119211).

Microscale Thermophoresis

Recombinant protein was labeled using the Monolith His-Tag Labeling Kit RED-tris-NTA (Nanotemper Technologies, MO-L018) following the manufacturer's protocol at a 1:2 dye to protein ratio, in a reaction with a final concentration of 100 nM labeled protein; this protein was determined by the BSA standard curve quantification. Labelling was assayed *via* a capillary scan at 60% LED power, and protein was diluted to 600 units using the Nanotemper-provided 1x PBST; this resulted in a target protein concentration of ~50 nM. Labeled protein was mixed with ligand and incubated for 5 minutes at room temperature before being loaded into Monolith NT.115 Capillaries or NT.115 Premium Capillaries (NanoTemper Technologies, MO-K022 and MO-K025). MST was measured using a Monolith NT.115 instrument (NanoTemper Technologies) at an ambient temperature of 25°C. Instrument parameters were 60% excitation power and Medium MST power. Data from at least three independently-pipetted measurements were analyzed (MO.Affinity Analysis software, NanoTemper Technologies) using the fraction bound as indicated in the respective figures. When indicated, labeled protein was pre-incubated with freshly prepared galactose (Sigma, G6404), glucose (Sigma, 49139), 3-O-methyl-D-glucopyranose (3MG, Sigma, M4879) or ATP (Promega, V915A) at room temperature for 10 minutes. The sequences for RNA are as follows: G4 RNA: 5'-GUU GGG GCG GGC GUU GGG UUU GGG GGG ACG-3'; CLIP-RNA: 5'-CAG UGG CUG CUG CUG UGG CCA CGU G-3'; Random-RNA: 5'-UUG GUA GUC ACC CCA AAU UGU UAU U-3'. For DDX21 dimerization, Flag-HA (FH) tagged of DDX21 is used for serious dilution.

Fluorescence-based binding assay

To prepare dye-conjugated glucose, 200 μM AZDye 488 Alkyne (Click ChemTools, 1277-1) was reacted with 400 μM 2-Azido-2-deoxy-D-glucose (Santa Cruz Biotechnology, sc-256068) in 1X PBS at room temperature for 1 hour with 0.1 mM $CuSO_4$, 0.5 mM THPTA and 15 mM sodium ascorbate. The reaction was checked for completeness by Thin Layer Chromatography (TLC) using acetonitrile buffer. Fluorescence was measured with 50 nM glucose conjugated AZDye 488 and a concentration gradient of FHH-DDX21 recombinant protein. Fluorescence intensity was measured on a Tecan Infinite M1000 with excitation at 470 nm and emission at 525 nm with 5 nm bandwidth, gain at 50, z-position at 26,000 μm and G-factor 1.02 using 384 well plates. Fluorescence decreased upon addition of DDX21. Total intensities were used to calculate K_d by (1) dividing the fluorescence value in each well by the 0 nM protein well of the same replicate, (2) multiplying by -1, then (3) adding the absolute value of the lowest intensity to make the lowest value zero, and (4) fitting a 1:1 binding curve to the data using the python package pybindingcurve.[54] A negative control was run against unconjugated AZDye 488 Alkyne (Click ChemTools, 1277-1) by adding 0.25 μM FHH-DDX21 recombinant protein. No decrease in total intensity was observed for the negative control.

Quantitative RT-PCR Expression Analysis

For quantitative RT-PCR (qRT-PCR), total RNA was extracted using RNeasy Plus (QIAGEN, 74136) and subsequently subjected to reverse transcription using the iScript cDNA Synthesis Kit (Bio-Rad, 1708891). qRT-PCR analysis was performed using the LightCycler 480 II System (Roche) with the SYBR Green Master Mix (Thermo Fishier, K0223). Samples were run in duplicate and normalized to levels of 60S ribosomal protein L32 for each reaction. The following primers were used for qPCR analysis:

Gene	Forward Primer	Reverse Primer
CDK1	TGCTTATGCAGGATTCCAGGTT	CATGTACTGACCAGGAGGGA
CDKN1A	GGGTCGAAAACGGCGGCAGA	CCTCGCGCTTCCAGGACTGC
DDX21	TGCCATCAGGCTTTTGGATT	GTCACAAAACCCACATTTGA
DNMT1	AAGCCCGTAGAGTGGGAATG	GCTAGGTGAAGGTTCAGGCTT
FLG	AAAGAGCTGAAGGAACTTCTGG	AACCATATCTGGGTCATCTGG

(*Continued on next page*)

Continued

Gene	Forward Primer	Reverse Primer
GRHL1	GCCTACCCACTCCATCAAGA	GAGTCTGGAGTTCGCCTTTG
GRHL3	GGTGTTCATCGGCGTAAACT	CCCAAGCCACAGTCATAGGT
IVL	TGCCTGAGCAAGAATGTGAG	TGCTCTGGGTTTTCTGCTTT
KRT1	GAAGTCTCGAGAAAGGGAGCA	ATGGGTTCTAGTGGAGGTATCTA
KRT10	GCAAATTGAGAGCCTGACTG	CAGTGGACACATTTCGAAGG
KLF4	TCCACAACTTCCAGTCACCC	AGAACAGATGGGGTCTGTGAC
LCE3D	GCTGCTTCCTGAACCAC	GGGAACTCATGCATCAAG
L32	AGGCATTGACAACAGGGTTC	GTTGCACATCAGCAGCACTT
MAF	TATGCCCAGTCCTGCCGCTT	CGCTGCTCGAGCCGTTTTCT
MAFB	GACGCAGCTCATTCAGCAG	CCGGAGTTGGCGAGTTTCT
S100A8	ATTTCCATGCCGTCTACAGG	CCAACTCTTTGAACCAGACG
ZNF750	AGCTCGCCTGAGTGTGAC	TGCAGACTCTGGCCTGTA

Western blot and Immunofluorescence

For immunoblot analysis, proteins were quantified by Bradford assay (Bio-Rad, 5000201). 10-20 μg of cell lysates were loaded per lane on an SDS-PAGE gel and transferred to a nitrocellulose membrane at 4°C. The resulting membrane was blocked with LI-COR blocking buffer (PBS) at room temperature for 1 hour. The membrane was then incubated with primary antibody at 4°C overnight. Membranes were washed with TBS-T and incubated with secondary goat anti-mouse and goat anti-rabbit antibodies (LI-COR Biosciences) at a dilution of 1:4,000 for 1 hour at room temperature. After incubation with secondary antibodies, membranes were washed with TBS-T and visualized using the Odyssey CLx Infrared Imaging System (LI-COR Biosciences). Quantification was performed using Licor ImageStudioLite software (LI-COR Biosciences).

For immunofluorescence staining, tissue sections (7 μm thick) were fixed using either acetone or methanol. Cell slides were fixed with 4% paraformaldehyde (Alfa Aesar, 43368). Primary antibodies were incubated at 4°C overnight, and secondary antibodies were incubated at room temperature for 1 hour. The nucleolus staining was proceeded by using Nucleolus Bright Red (Dojindo, N512-10). Nuclear was stained by Duolink® In Situ Mounting Medium with DAPI (Sigma, DUO82040-5ML). All images were taken and processed using a Zeiss microscope with ApoTome.2 or Zeiss LSM880 confocal microscope.

The antibodies used in this study include anti-DDX21 (ProteinTech, 10528-1-AP), ms-anti-HA (Abcam, ab130275), Rb-anti-HA (CST, #3724), anti-HNRNPUL1 (MyBioSource, MBS2524350), anti-HNRNPC (Santa Cruz Biotechnology, sc-32308), anti-HNRNPF/H (Santa Cruz Biotechnology, sc-32310), anti-V5 (CST, #13202), anti-HNRNPA2B1 (Santa Cruz Biotechnology, sc-374053), anti-Actin (Sigma, A2228), anti-H3 (CST, #14269), anti-Fibrillarin (CST, #2639), anti-Tubulin (Sigma, T9026), anti-Strept (LI-COR, 926-32230), anti-KRT1 (Covance, PRB-149P), anti-KRT10 (Neomarkers, MS611P), anti-Ki67 (Neomarkers, SP6), ms-anti-CollagenVII (Chemicon, MAB1345) and pAb-anti-CollagenVII (Chemicon, 234192).

ATPase Activity Assay

ATPase activity assay was done by using the ADP-Glo kinase assay kit (Promega, V6930) following the manufacturer's protocol. Each reaction contained 75 ng (final ~25 nM) DDX21 WT, K236R or K236G, or, in the negative control, 75 ng BSA. Luminescence signal was measured on a Tecan Infinite M1000 Pro with 630 ms integration time using 96-well plates; signal was normalized to the BSA control.

Helicase Unwinding Assay

The helicase unwinding assay was performed following published methods.[55] The unwinding assay step was at 37°C for 30 minutes with 150 nM recombinant DDX21, in unwinding buffer (20 mM Tris-acetate, pH 7.5, 2 mM magnesium acetate, 100 mM KCl) with 1 mM ATP (Promega, V915A), 20 U RiboLock RNase Inhibitor (Thermo Fishier, EO0381) in a total volume of 50 μL, with or without galactose or glucose (oligos and concentrations were 30 nM Cy3-RNA: Cy3-GUU UUU CAA UUU UUU ACU UUU UUC; and 45 nM BHQ-RNA: GAA CAA CAA CAA CAA CCA UGG AAA AAA GUA AAA AAU UGA AAA AC-BHQ2; 200 nM complement DNA: GAA AAA AGT AAA AAA TTG AAA AAC;). Fluorescence intensity was measured using a Tecan Infinite M1000 Pro with excitation at 550 nm and emission at 570 nm with 5 nm bandwidth, gain at 100 and z-position at 20,000 μm using 96-well plates.

CellTiter-Blue (CTB) Cell Viability Assay

Before measuring viability, 2,000 keratinocyte cells were seeded in 24-well plates and cultured for indicated time. Cell proliferation was measured using the CellTiter Blue Cell Viability Assay (Promega, G8080) according to the manufacturer's instructions. Fluorescence intensity was measured using a SpectraMax M5 plate reader with excitation at 555 nm and emission at 585 nm with cutoff at 570 nm.

TUNEL Assay

Terminal deoxynucleotidyl transferase dUTP nick end labeling (TUNEL) assay was performed with In Situ Cell Death Detection Kit, TMR red (Sigma, 12156792910) following manufacturer's protocol to detect cell death in 3D organotypic human epidermal tissues culture. All images were taken and processed using a Zeiss microscope with ApoTome.2.

RNA-seq

For RNA-seq, total RNA was extracted using the RNeasy Plus kit (QIAGEN, 74136) and libraries were prepared with QuantSeq 3′ mRNA-Seq Library Prep Kit FWD for Illumina (Lexogen, 015.96) following manufacturer's protocol. RNA-seq was performed on a NovaSeq 6000, paired-end, 150 bp length, with ~30 M reads for each sample.

For mRNA-seq splicing analysis, total RNA was extracted using the RNeasy Plus kit (QIAGEN, 74136), followed by poly(A) enrichment and library preparation using the NEB Ultra II (non-directional) kit (E6111). Libraries were sequenced on a NovaSeq 6000, paired-end, 150 bp length, with ~30 M reads for each sample.

Nucleolus Fractionation

Cells were washed with PBS and resuspended in 500 μL of ice-cold Buffer A (10 mM HEPES, pH 7.9, 1.5 mM $MgCl_2$, 10 mM KCl, 0.5 mM DTT, 1X protease inhibitor). Cells were incubated on ice for 5 minutes before resuspended pellets were transferred into a pre-chilled 2 ml Dounce homogenizer (Type A) with 10 strokes of a tight pestle. Dounced cells were centrifuged for 5 mins,1000 rpm at 4°C with supernatant retained as cytoplasmic fraction. Pellets were resuspended in 3 mL of S1 (0.25 M Sucrose, 10 mM $MgCl_2$) and layered over a 300 μL cushion of S2 (0.35 M Sucrose, 0.5 mM $MgCl_2$) by slowly pipetting the S1 solution on top of S2. The sucrose solutions were centrifuged for 5 minutes at 4°C, 2500 rpm. Supernatants were removed and pellets resuspended in 300 μL of S2 (0.35 M Sucrose, 0.5 mM $MgCl_2$) before sonication at 50% amplitude for 10 secs, with a 10 sec rest on ice between each sonication, using a probe sonicator (Branson Digital Sonifier). Sonication was continued until isolated nucleoli were observed by microscopy. Sonicated samples were layered over 300 μL S3 (0.88 M Sucrose, 0.5 mM $MgCl_2$), again by pipetting the solution slowly on top of the S3 layer. Samples were centrifuged for 10 minutes at 4°C, 3,500 rpm. Supernatant were retained as nucleoplasmic fractions. Pellets were washed by resuspending them in 500 μl of S2 (0.35 M Sucrose, 0.5 mM $MgCl_2$) and centrifuging for 5 mins at 4°C, 3500 rpm. This final pellet was retained as the nucleoli fraction. All fractions were subjected to Western blot analysis.

High Molecular Weight Fractionation

Nuclei from cell cultures were purified as using 5 volumes of buffer A (10 mM HEPES, pH 7.5, 10 mM KCl, 1.5 mM $MgCl_2$, 1 mM DTT, 1X protease inhibitors) on ice for 1-2 min before adding an equal volume of buffer B (10 mM HEPES, pH 7.5, 10 mM KCl, 1.5 mM $MgCl_2$, 1 mM DTT, 0.4% NP-40, 1X protease inhibitors), and performing an additional incubation on ice for 3-4 min. Nuclei were then collected by centrifuging at 4,000 rpm for 1 minute and were lysed for 5 minutes in 5-10 volumes of ice-cold lysis buffer (20 mM HEPES, pH 7.5, 150 mM NaCl, 1.5 mM $MgCl_2$, 0.5 mM DTT, 1X protease inhibitors, and 0.6% Triton X-100). Soluble and HMW fractions were separated by centrifugation at max speed for 5 minutes at 4°C. The soluble fraction was removed, and an equal volume of lysis buffer was added to the HMW pellet. Soluble and HMW fractions were rotated at 25°C on with 2.5 U/μl of Benzonase (Sigma, E1014-25KU) until the HMW pellet was resuspended (~30 min) and then clarified by centrifugation for 10 minutes at max speed, 4°C.

Blue Native Gel

Blue Native Gels were run using NativePAGE™ 4 to 16%, Bis-Tris gels (Invitrogen, BN1004BOX), following the manufacturer's protocol. 300 ng of recombinant DDX21 WT and 611R mutant were incubated at room temperature for 15 minutes with or without 350 μM glucose or galactose in 1X PBS. Samples were mixed with 4X Sample Buffer (Invitrogen, BN2003), adding 5% G-250 Sample Additive (Invitrogen, BN2004). Blue native gels were run following the manufacturer's protocol (dark blue buffer for 30 minutes, changed to light blue buffer and run until proteins reached the end). Gels were subjected to either silver stain (Pierce, #24612) or Western blot analysis following the manufacturer's protocol. Gels were transferred to PVDF membranes and washed with 100% methanol until all blue dye was removed, after which the blocking and antibody incubations were performed as described above.

Nanoscale Secondary Ion Mass Spectrometry (NanoSIMS)

Keratinocyte cells were seeded on 7 mm × 7 mm silicon substrates (coated with VECTABOND® Reagent, Vector Laboratories, SP-1800-7) for progenitor (5% confluency seeding) and differentiated cell culture (100% confluency seeding). Cells were maintained in 50% (v:v) complete Keratinocyte-SFM (Gibco, #17005-142) and 50% (v:v) Medium 154 (Gibco, #M-154-500) without adding extra $CaCl_2$ for 2 days. After 2 days, cells were incubated with 100 μM D_4 ATP (Cambrige Isotope Lab, DLM-8922-CA-20) and 2.25 g/L $^{13}C_6$ glucose (Sigma, #389374) in 50% (v:v) glucose-free DMEM supplied with SFM supplement and 1X Sodium Pyruvate, 25% (v:v) complete Keratinocyte-SFM (Life Technologies, #17005-142) and 25% (v:v) Medium 154CF (Gibco, # M154CF500) for 20 hours. Control cells were incubated with the same concentration of light ATP and light glucose. After 20 hours, progenitor and day 3 differentiated cells on silicon substrates were washed with 150 mM ammonium acetate solution (pH 7.3), followed by drying in a vacuum desiccator at room temperature overnight and imaging immediately afterwards. Organoid tissue is cultured in normal KGM for 5 days and then switched to KGM supplied with $^{13}C_6$ glucose in glucose free DMEM (final $^{13}C_6$ glucose concentration in

KGM is 4 g/L) and dialyzed-FBS (replace characterized FBS in KGM) for 40 hours before harvesting. Tissue sections (7 μm thick) were lyophilized overnight and subjected to the next step immediately. The cells and organoid tissues on silicon substrates were then coated with ~20 nm Au and loaded into the SIMS device for ion imaging.

Samples were loaded into a Cameca NanoSIMS 50L ion microprobe and were pumped down to ultra-high vacuum ($<10^{-9}$ Torr) for mass spectrometry analysis. Ion imaging was conducted using a Cs^+ primary beam set to 15pA current for cells, and 5pA current for tissue samples. Seven electron multiplier detectors were set to simultaneously collect the masses of $^2H^-$, $^{12}C^-$, $^{13}C^-$, $^{16}O^-$, $^{28}Si^-$, $^{31}P^-$, and $^{12}C^{14}N^-$ or $^{12}C_2^-$, using a mass resolution M/ΔM > 4300, sufficient to resolve isobaric interferences such as $^{30}SiH^-$ on $^{31}P^-$. In addition, a secondary electron image was captured at each scan. Cells were pre-sputtered for 2 min at 50-150pA to remove gold coating and surface contamination prior to analysis. Once a region of interest (ROI) was defined, a 35 μm × 35 μm or 30 μm × 30 μm subcellular area was scanned 500-1,000 frames for cells, typically taking 9-18 h of image acquisition per region. For tissue sections, a 70 μm × 70 μm area was scanned for 61 frames. Data were visualized using Cameca's WinImage software and analyzed by WinImage and Python. The total counts from frames 100-500 or 200-500 (for cells), and 1-61 (for tissues) were accumulated for image analysis. The summed ^{12}C and ^{13}C counts were used to normalize the counts of other isotopes.

Proximity Ligation Assay (PLA)

Protein protein interaction in living cells was measured by PLA with Duolink® In Situ Orange Starter Kit Mouse/Rabbit (DUO92102-1KT) according to the manufacturer's instructions. Briefly, FHH-tagged $DDX21^{WT}$ and V5-tagged corresponding interacting protein were both expressed to endogenous levels in keratinocyte progenitors and cultured the cells in different conditions as indicated. Anti-HA (ThermoFisher, #26183) and anti-V5 (CST, #13202) antibodies were applied for PLA primary antibody incubation. After Duolink® PLA probe incubation, ligation, and amplification, PLA samples were imaged by a Zeiss microscope with ApoTome.2.

Azido-glucose Pulldown-MS

Azido-glucose pulldown-MS experiment was performed following previous protocol.[7] Briefly, keratinocytes were seeded for differentiation at full confluence in 6-well plates and grown for 2.5 days at which point media was changed from normal glucose (4.5 g/L) DMEM to a mix of 2.25 g/L 2-azido-2-deoxy-D-glucose and 2.25 g/L D-glucose DMEM and incubated for 15 hours (for control, treat cells with 4.5 g/L D-glucose DMEM). Cells were washed with PBS twice, crosslinked by UVC (254 nm, UV Stratalinker 2400) at 0.3 J/cm^2 then lysed in urea lysis buffer (200 mM Tris pH8, 4% CHAPS, 1 M NaCl, 8 M Urea). The Click-&-Go Click Chemistry Capture Kit (Click Chemistry Tools, #1065) was used to isolate azido-glucose linked proteins according to the manufacturer's instructions. Samples were digested on-bead per the kit protocol and sent for LC-MS/MS analysis on an Orbitrap Fusion mass spectrometer. The parameter for mass spectrometry analysis and database search was following previously published protocol using Preview and Byonic v2.6.49 (ProteinMetrics).[7]

Spectral match assignment files collapsed to the gene level and false positive matches and contaminants were removed. SAINT analysis[56] (crapome.org) was run with the following parameters: 10,000 iterations, LowMode ON, Normalize ON and the union of MinFold ON and OFF. Minimum interactome inclusion criteria were SAINT ≥ 0.8, fold change over control ≥ 2.

BioID, UVC Crosslinking and BS3 Crosslinking

BioID in HEK293T cells was performed with transient transfections of wild type DDX21 and K236R, K236G, or 611R mutants expressed at endogenous levels, using BASU-NLS-GFP as the control. In keratinocytes, bioID was performed with cells containing stable virus integrations of wild type DDX21 at endogenous levels or, as the control, uORF-BASU-NLS-GFP. Cells were labeled with 100 μM biotin for 5-6 hours and harvested by washing twice with 1X ice cold PBS and lysed on ice for 30 minutes (50 mM Tris-HCl pH 7.5, 300 mM NaCl, 1 mM EDTA, 1% Triton X-100, 1X Protease Inhibitor Cocktail), and sonicated for 3 cycles of 10 s at 10% amplitude, followed by 10 s pauses. After sonication, cell lysates were centrifuged through a 3 kDa filter (Millipore, UFC900324) to remove excess biotin and to exchange the buffer to 50 mM Tris-HCl pH 7.5, 500 mM NaCl, 0.2% SDS, containing 1X Protease Inhibitor Cocktail. Cell lysates were incubated with MagReSyn Streptavidin beads (Resyn Biosciences, MR-STV010) with 25 μL of beads *per* mg of lysate for 2 hours at room temperature or overnight at 4°C. Beads were then washed with buffer 1 (3% LDS) twice, buffer 2 (50 mM HEPES, pH = 7.5, 500 mM NaCl, 1 mM EDTA, 0.1% Na-DOC, 1% TritonX-100) once and buffer 3 (10 mM Tris-HCl pH = 7.5, 250 mM LiCl, 1 mM EDTA, 0.5% Na-DOC, 0.5% NP-40) once, with a final wash of 50 mM Tris-HCl pH 7.5. After washing, beads were then subjected to on-bead digestion for HEK293T samples or in-gel digestion for keratinocyte samples.

For UVC crosslinking samples, DDX21 recombinant protein (20 ng/μL) was incubated with or without 350 μM glucose at room temperature for 15 minutes and was crosslinked by UVC (254 nm, UV Stratalinker 2400) at 0.3 J/cm^2 in 1.5 μL droplets on a parafilm, cross-linking a total of 20 droplets per sample. All 20 droplets for each sample were combined for in-gel digestion.

For BS3 crosslinking samples, DDX21 recombinant protein (50 ng/μL) was incubated with or without 1 mM ATP (Promega, V915A) or 350 μM glucose at room temperature for 15 min and was crosslinked following published protocol[57] by 10 μM BS3 (ThermoFisher, #21580) at room temperature for 1 hour and then quenched by adding LDS sample loading buffer (Invitrogen, NP0008). Cross-linked protein was then subjected to in-gel digestion.

Sample Preparation and LC-MS/MS Analysis

For on-bead digestion, bead-captured protein was reduced with dithiothreitol and alkylated with iodoacetamide. Processed proteins were subsequently digested overnight with Trypsin/Lys-C (Promega, V5071) at an enzyme/substrate ratio of 1:100 in 50 mM NH_4HCO_3 (pH 8.5) at 37°C. For in-gel digestion, samples were loaded onto a 10% SDS-PAGE gel. After electrophoresis, the desired gels were cut into slices, reduced in-gel with dithiothreitol, and alkylated with iodoacetamide. Processed proteins were subsequently digested in-gel, overnight, with Trypsin/Lys-C (Promega, V5071) at an enzyme/substrate ratio of 1:100 in 50 mM NH_4HCO_3 (pH 8.5) at 37°C. The next day, peptides were recovered from gels first using a solution containing 5% acetic acid in H_2O and second with a solution containing 2.5% acetic acid in an equal volume mixture of CH_3CN and H_2O.

All the resulting peptide mixture was subsequently dried in a Speed-vac and desalted using OMIX C18 pipet tips (Agilent Technologies, A57003100). LC-MS/MS experiments were conducted on a Q Exactive Plus mass spectrometer equipped with an UltiMate 3000 UPLC system (Thermo Fisher Scientific).

Samples were automatically loaded at 3 μL/min onto a precolumn (150 μm i.d. and 3.5 cm in length) packed with ReproSil-Pur 120 C18-AQ stationary-phase material (5 μm in particle size, 120 Å in pore size, Dr. Maisch). The precolumn was connected to a 20-cm fused-silica analytical column (PicoTip Emitter, New Objective, 75 μm i.d.) packed with 3 μm C18 beads (ReproSil-Pur 120 C18-AQ, Dr. Maisch). Peptides were then resolved using a 180-min gradient of 2-45% acetonitrile in 0.1% formic acid. The flow rate was maintained at 300 nL/min.

The mass spectrometer was operated in a data-dependent acquisition mode. Full-scan mass spectra were acquired in the range of *m/z* 350-1500 using the Orbitrap analyzer at a resolution of 70,000 at *m/z* 200. Up to the 25 most abundant ions found in MS with a charge state of 2 or above were sequentially isolated and collisionally activated in the HCD cell with a normalized collision energy of 28 to yield MS/MS.

Mass Spectrometry Data Analysis

For bioID in HEK293T cells, Maxquant (v. 2.0.1.0) was used to analyze the LC-MS and MS/MS data for protein identification and quantification in LFQ mode,[58] searching against the human Uniprot database, Proteome ID UP000005640 (reviewed and with isoforms). For bioID in keratinocytes, Maxquant (v. 1.5.2.8) was used to analyze the LC-MS and MS/MS data for protein identification and quantification in LFQ mode,[58] searching against the human IPI database, version 3.68, containing 87,061 protein entries. Label-free quantification was applied for all bioID searches. The maximum number of miss-cleavages for trypsin was two per peptide. Cysteine carbamidomethylation and methionine oxidation were set as fixed and variable modifications, respectively. The tolerances in mass accuracy were 20 ppm for both MS and MS/MS. The maximum false discovery rates (FDRs) were set at 0.01 at both peptide and protein levels, and the minimum required peptide length was 6 amino acids. Ratios were calculated from normalizing the intensity to the BASU-NLS-GFP control for each condition in each biological replicate.

For BS3 crosslinking-MS, raw files were first converted to *.mgf format with RawConverter (v. 1.2.0.1) and then files were searched by XiSearch (v. 1.7.6.1) using mass accuracy tolerances of 20 ppm[59] and filtered by XiFDR (v. 2.1.5.2) with the FDR setting as recommended.[60]

For UVC crosslinking-MS, raw files were first searched by Maxquant (v. 2.0.1.0) using the same search parameter as indicated above, searching against DDX21 protein sequence FASTA. 57 unique peptides were quantified and examined manually to identify if any were glucose crosslinked or not by adding glucose, glucose losing H_2O or glucose losing NH_3 for selected ion chromatography (SIC), MS and MS/MS.

Homology Directed Repair Genome Editing (HDR)

Vector construction

The donor ssAAV vector used as a template for HDR was constructed by cloning ~1200bp genomic DNA sequence flanking the 5' and 3' end of the target mutation into the AAV transfer plasmid between AAV ITR sequences. For each editing experiment, two consecutive constructs were generated that differ by presence of the mutation of interest or a synonymous substitution control. During genomic amplification, the following point mutations were engineered: K236K (AAG/AAA), K236R (AAG/AGG), K236G (AAG/GGC) within exon 4, and domain synonymous substitution L611-L616 (CTGGCAGCAGCACTGGCC/CTGGCAGCAGCACTCGCC) as well as L611-L616/R611-R616 (CTGGCAGCAGCACTGGCC/CGGAGAAGAAGACGGCGC) within exon 12 of the targeted DDX21 gene. Additionally, in order to prevent endonuclease mediated re-cutting, the following PAM mutations were engineered, resulting in synonymous amino acid substitutions: G/A in exon 4 (Q229Q), and G/C (L615L) in exon 12. For genomic DNA amplification, the following primers were used:

236F: 5'-ATCAACGCGTGCTAGCAAAGCTTTTTCAGGCCCTCTGT-3'
236R: 5'-GCTTGATATCGAATTCGAACCCAATGGACTCACCCT-3'
611-616F: 5'-ATCAACGCGTGCTAGCGGGACAAAGATGCTGGTGGTA-3'
611-616R: 5'-GCTTGATATCGAATTCAATTAGTACGAACAGTCCCTCGT-3'

Primers contained homology arms to the AAV transfer vector allowing In-Fusion assembly into NheI/EoRI digested AAV plasmid. After confirmation of the insert sequence integrity, constructs were used for AAV virus production at the Stanford Neuroscience Gene

Vector and Virus Core. AAV-DJ serotyped donor ssAAV virus was produced at genomic titer of 1.5-5x10^{13} TU/mL and used for HDR experiments at MOI 2.5x10^{5}.

CRISPR and AAV mediated HDR

The guide sequences targeting DDX21 for CRISPR/Cas9 genome editing were predicted using the CHOPCHOP web tool[61] and were ordered from IDT as sgRNA. The following gRNAs were used in this study:

gRNA for K236K: 5'-CGGGAAGGACTTAATTGCAC-3'
gRNA for L611-L616: 5'-GGAAGCTCTGGCAGCAGCAC-3'

For CRISPR/Cas9 genome editing, 73 pmol of sgRNA was complexed with 61 pmol recombinant Alt-RspCas9 protein (IDT) in 10 μL of Human Keratinocyte Nucleofector™ Kit solution (Lonza, VPD-1002) for 10 min and immediately used for nucleofection of 8x10^{5} primary keratinocytes with the Amaxa nucleofection apparatus (Lonza) using program T-018. After recovery, cells were mixed with AAV virus containing either wild type (WT) or mutant donor template at MOI 2.5x10^{5}, split into 2 wells of a 6-well plate and propagated for 72 hrs. After the culture reached 50-60% confluence, cells were grown in 10 cm plates, during which time genomic DNA was isolated and evaluated for the editing efficiency using PCR amplification and sequencing of the bulk cell population, as well as by cloning of the amplified fragment into a pBluescript vector and evaluating editing efficiency by individual colony sequencing. The population of cells with at least 75% editing efficiency were used for further experiments.

Fast Protein Liquid Chromatography (FPLC)

Cell from two 10 cm plates (70% confluency) were harvested, washed with ice cold PBS and lysed as indicated above in the high molecular weight fractionation section, except that DTT was excluded from buffers A and B. Protein complexes in the high molecular weight fraction were separated with a Superose 6 Increase 10/300 column (Cytiva 29-0915-96, 10/300 GL) on a AKTA Pure protein purification system attached to the fraction collector F9-C. The column was equilibrated with two column volumes of elution buffer (50 mM Tris-HCl pH 7.5, 300 mM NaCl, 10% Glycerol, 0.1% NP-40) and then run using one column volume of elution buffer after sample loading (200 μL loop) to elute protein complexes. Automatic sample collection was set to 250 μL/fraction. A mixture of thyroglobulin, g-globulin, ovalbumin, myoglobin, and vitamin B12 was used as gel filtration standards (BioRad, #1511901). For those samples indicated with glucose incubation, high molecular fractions were incubated with 350 μM glucose at room temperature for 20 min during benzonase treatment.

Immunoprecipitation

Approximately 3 million cells were harvested and washed with ice-cold PBS. Nuclei from harvested cells were purified as indicated above in the high molecular weight fractionation section and lysed with nuclear lysis buffer (50 mM Tris-HCl pH 7.5, 250 mM NaCl, 10% Glycerol, 0.1% NP-40, 1X protease inhibitor) on ice 20-30 for minutes with occasional vortexing. Lysates were passed through 27.5g needles and centrifuged for 15 minutes at 13,200 rpm, at 4°C. ~200 μg protein from this resulting nuclear lysate was combined with an equal volume of Tris buffer (50 mM Tris-HCl pH 7.5, 1X protease inhibitor) for a final concentration of ~1 mg/mL protein. Normalized nuclear lysates were combined with with 2 μg of either anti-HA (CST, #3724) or IgG (CST, #2729) and rotated at 4°C overnight. Lysates were further incubated with 20 μL protein G dynabeads (Invitrogen, 10004D) for 2 hours at 4°C and beads washed three times with wash buffer (50mM Tris-HCl pH 7.5, 150 mM NaCl, 0.01% NP-40). After washing, beads were boiled with sample buffer and analyzed by Western blot.

CLIP-seq

CLIP-seq on DDX21 in differentiated keratinocytes under low or normal glucose conditions was performed according to the published easyCLIP protocol.[33] Briefly, L3 adapters were of the form BBB AGA TCG GAA GAG CGG TTC AGA AAA AAA AAA AA/iAzideN/A AAA AAA AAA AA/3Bio/ where BBB denotes a barcode, /iAzideN/ denotes an internal azide group for dye conjugation, and /3Bio/ denotes a 3' biotinylation blocking group. L3 adapters were pre-adenylated and conjugated to DBCO-dyes before usage. L3 barcodes TCA, AGT and AAC were used to mark replicates 1, 2 and 3, respectively. L5 adapters were of the form /5AzideN/CT TGT GTG TGT GAA GCG AAG GGT ABB BBB BrNrN rNrNrN rNrN, where /5AzideN/ denotes a 5' azide group for dye conjugation, B denotes a barcode, and rN denotes random RNA bases to serve as a UMI. L5 barcodes CGATTA and AGCTAG were used to mark low and high glucose samples, respectively. Keratinocytes were washed once with ice cold PBS and UVC cross-linked at 254 nm in 6-well plates in a Stratalinker at 0.3 J/cm2. After cross-linking, cells were harvested in ~1 mL 4° CLIP lysis buffer per replicate. Roughly 2 mg clarified lysate per replicate was combined with 22 μL anti-HA magnetic beads (ThermoFisher #88837), incubated for one hour, washed, treated with 0.02 U/μL Ambion RNAse I (ThermoFisher, #AM2294) at 30° for ~3 minutes, 3' dephosphorylated with PNK and ligated overnight to the L3 adapters. After L3 adapter ligation, replicates were combined, 5' phosphorylated, and ligated to the L5 oligos. All samples were then combined before running on an SDS-PAGE gel, transferring to nitrocellulose, RNA extracted, reverse transcribed and PCR amplified. CLIP-seq sequencing was performed on a HiSeq, paired-end, 150 bp length, with ~35 M reads for each sample.

HEK293T cells were stable integrated of wild type DDX21 and K236R, K236G, or 611R mutants at endogenous levels with virus, and CLIP-seq samples were processed with the updated CLIP-seq protocol.[62] This method differs principally in adapter sequences. L3

adapters were of the form /5Phos/rNrNrN rNrNB BBB BAG ATC GGA AGA GCA CAC GTC AAA AAA AAA AAA AAA AAA AAA AAA/3AzideN/, where /5Phos/ denotes 5' phosphyorylation, rN denotes random RNA bases that form a UMI, B denotes a barcode, and /3AzideN/ denotes a 3' terminal azide blocking group for dye conjugation. These L3 adapters were not pre-adenylated, and instead the 3' ligation was run identically as the L5 ligation, except with the L3 adapter – that is, ATP was present for the ligase to adenylate the L3 oligos. L5 oligos were of the form /5AzideN/TCG GCA GCG TCA GAT GTG TAT AAG AGA CAG BBB BBB rNrNrN rNrNrN rN, where /5AzideN/ denotes a 5' terminal azide blocking group for dye conjugation, B denotes a barcode, and rN denotes random RNA bases forming a UMI. The updated library preparation protocol was similar except the L3 adapter was ligated in the same ATP-containing conditions as the L5 adapter, the RT primer was changed to GTT CAG ACG TGT GCT CTT CCG ATC T, and the PCR was performed differently. Specifically, after an initial 15-cycle PCR with short primers (TCG TCG GCA GCG TCA GAT GTG TAT AAG AGA CAG and GTG ACT GGA GTT CAG ACG TGT GCT CTT CCG ATC T, which are Nextera and TruSeq sequencing primers, respectively), PCR product was purified by AMPure XP beads (Beckman, #A63880), run on a 4% agarose E-Gel with SYBR Safe DNA Gel Stain (ThermoFisher, A42136), purified with a Qiagen gel extraction kit (Qiagen, #28706X4), input into a second PCR with standard barcoded Nextera and TruSeq primers, amplified for 4-5 cycles, and finally purified with AMPure beads to complete the library preparation. 293T cells were washed with 4°C PBS and cross-linked in 15 cm plates in a Stratalinker at 0.3 J/cm^2, then harvested in 1 mL CLIP lysis buffer per plate. ~10 mg clarified lysate per replicate from 293T cells expressing HA-tagged wild-type or mutant DDX21 were combined with 22 μL anti-HA magnetic beads (ThermoFisher, #88837), incubated for one hour, washed, treated with 0.02 U/μL Ambion RNAse I (ThermoFisher #AM2294) at 30°C for ~3 minutes, and processed according to the updated easyCLIP protocol. For DDX21 CLIP-seq from progenitor keratinocytes, the same conditions were used except ~2 mg of clarified lysate was used per replicate.

CUT&RUN-seq

CUT&RUN was performed on 0.5-1 million primary keratinocytes according to the EpiCypher protocol ("CUT&RUN Protocol v2.0", revised 3/15/2022) and kit (EpiCypher, 14-1048), either using antibody to the endogenous DDX21 or infected with virus expressing HA-tagged DDX21. Two independent experiments with unrelated donors using 2-3 replicates per donor were performed with HA-tagged DDX21 and two replicates of one donor were used for endogenous DDX21. Progenitor cells were not cross-linked, while differentiated cells were cross-linked, as this yielded a reduction in bead aggregation after nuclear extraction. Keratinocytes were washed with PBS, harvested with trypsin and cross-linked in media with 0.1% formaldehyde for 1 minute before quenching with 125 mM glycine. After quenching, cells were placed on ice, centrifuged at 4°C, washed with cold PBS + 0.1% BSA, and maintained afterwards at 4°C. Nuclei were extracted by resuspending in 100 μL nuclei extraction buffer per 2.5 million cells (20 mM HEPES pH 7.5, 10 mM NaCl, 0.5 mM spermidine, 0.1% BSA, 0.1% NP-40, and 1 tablet Roche protease inhibitor per 10-20 mL) and incubating for 10 minutes on ice. 5-10 volumes of wash buffer were added, cells centrifuged, resuspended in wash buffer, and quantified using a Countess. Nuclei were bound to 10 μL activated Concanavalin A beads (EpiCypher, 21-1401) per sample, stained at 4°C for 2 hrs to overnight with 1:50 antibody dilutions (anti-HA, CST, #3724; anti-DDX21, ProteinTech, 10528-1-AP; anti-DDX21, Novus Biologicals, NBP1-83310; IgG, CST, #2729; anti-H3K27me3, Active Motif, 39055), washed, and incubated with 2.5 μL pAG-MNase (EpiCypher, 15-1016) per sample for 1 hour at 4°C with rocking, washed, digested for 15-30 minutes, and reactions quenched with EpiCypher STOP buffer for 30 minutes at 37°C according to the manufacturer's protocol. Nuclei and beads were centrifuged for >4,800 rcf at 4°C for 5-15 minutes, placed on a magnet, and supernatant containing released fragments was removed. Cross-links were then reversed by the addition of SDS to ~0.2% and proteinase K to ~0.4 μg/mL (final concentrations), incubating for 55°C in a thermomixer for 4 hours to overnight. DNA was extracted by a Zymo DNA Clean and Concentrator (Zymo Research, D4014), eluting in 27 μL water. Library was prepared using the NEB Ultra II DNA library prep kit (NEB, E7103S) following the manufacturer's protocol with modifications according to published research.[63] CUT&RUN-seq sequencing was performed on a NovaSeq 6000, paired-end, 150 bp length, with 15-20 M reads for each sample.

Chromatin Fractionation

Chromatin fractionation was performed according to published methods.[64] Approximately two million primary keratinocytes were harvested and washed twice with PBS. Cells were lysed with buffer A (10 mM Tris-HCl pH 8.0, 0.34 M sucrose, 3 mM CaCl2, 2 mM MgCl2, 0.1 mM EDTA, 1mM DTT, 0.5% NP-40, 1X protease inhibitor) on ice for 30 minutes followed by centrifugation at 5,000 rpm for 2 minutes at 4°C. Supernatants from this centrifugation were retained as S1 fractions and the pellet was subjected to nuclei lysis using buffer B (20 mM HEPES pH 7.5, 1.5 mM $MgCl_2$, 150 mM KCl, 0.1% NP-40, 1mM DTT, 10% Glycerol, 1X protease inhibitor). The nuclear lysate was centrifuged at 13,200 rpm for 30 minutes at 4°C. The supernatant of this centrifugation was retained as the S2 fraction; the protein in the pellet was released by adding buffer C (20 mM HEPES pH 7.5, 1.5 mM $MgCl_2$, 150 mM KCl, 10% Glycerol, 1X protease inhibitor and 0.5 U/μl of Benzonase [Sigma, E1014-25KU]) and incubating on ice for 1.5 hours, pipetting every 10 minutes. This mixture was centrifuged at 5,000 rpm for 2 minutes at 4°C, retaining its benzonase-released supernatant as S3. Fractions S1 and S2 were combined to form the SF (soluble fraction), and S3 as CF (chromatin fraction).

Sequencing Data Analysis

CUT&RUN-seq analysis

Cutadapt[65] (v. 1.8.1) was used to remove NEBNext/TruSeq adapters (AGA TCG GAA GAG CAC ACG TCT GAA CTC CAG TCA and AGA TCG GAA GAG CGT CGT GTA GGG AAA GAG TGT). Bowtie2[66] (v. 2.4.2) was used to map clipped reads to the hg38 genome,

using the parameters –end-to-end –very-sensitive –no-mixed –no-discordant -I 10 -X 700. Samtools was then used to add mate score tags (samtools fixmate -m), sort, mark duplicates (samtools markdup), and filter out unmapped reads and optical duplicates (samtools view -f 3 -F 1024). For visualization, reads-per-million scaled bigwig files created separately for each set of replicates (that is, two sets of HA-tagged DDX21, one set of endogenous DDX21) were averaged with equal weight to each replicate. MACS2[67,68] (v. 2.2.71) was run on the filtered bam files, controlling CUT&RUN samples to IgG samples, using the default parameters plus -f BAMPE –bdg. Peak regions across all samples were merged using bedtools[69] merge.

Hexamer-primed RNA-seq analysis

GRCh38 ENSEMBL v.104 annotations and the GRCh38 genome sequence were downloaded from ENSEMBL. STAR[70] (v. 2.7.8a) was used to generate an index from these files and map raw, paired-end, fastq files with the parameter "—quantMode TranscriptomeSAM", which outputs both chromosomal-coordinate bam files and *.toTranscriptome.out.bam files in transcript coordinates. Transcriptome-aligned bam files were passed to the RSEM[71] (v. 1.3.3) program rsem-calculate-expression to generate read counts per transcript.

Differential exon analysis

Transcript isoforms in the genome annotation file were filtered to remove isoforms comprising less than 0.05% of all isoforms.[72] Rsubread[73] (v. 2.0.1) was run on the chromosomal-coordinate bam files with the pre-filtered GTF file to generate counts per exon, using the function featureCounts. The exons counts generated by Rsubread were passed to DEXSeq[74] (v. 1.32.0, R version 3.6) to generate exon fold-changes and significances using the default parameters and the design formula ~ sample + (exon + batch) * condition, where batch represents the group of samples processed together and condition represents the group to be compared (e.g., low glucose).

Differential event-based splicing analysis

ENSEMBL v.104 annotations were used to define possible splicing events by rMATS turbo (v. 4.1.1) according to the author's suggested pipeline.[36] Statistics were calculated by rMATS without the "–paired" option. In Figure 7C, all events reported by rMATS were included, without filtering. Elsewhere, a 100 minimum read count cutoff was used.

Differential intron analysis

IRFinder[75] (v. 1.3.0) was used to build a reference genome based on the same ENSEMBL v.104 GTF used for STAR mapping. IRFinder was run on the chromosomal coordinate bam files with the default parameters, following the author's suggested pipeline of running on both individual replicates and bam files with replicates combined. The IRFinder analysis script analysisWithLowReplicates.pl was then run to determine fold changes and significances, which applies an Audic and Claverie test.[75,76] P-values reported by IRFinder were converted to Benjamini/Hochberg FDR values to control for multiple hypothesis testing. To control for batch effects between the two batches of anti-DDX21 shRNA relative to control shRNA, significances were first calculated on individual replicates relative to their respective control replicate within their batch using the IRFinder analysis script analysisWithNoReplicates.pl, following IRFinder guidelines, which also applies an Audic and Calverie test. P values were then combined using Fisher's method and converted to Benjamini/Hochberg FDR values to control for multiple hypothesis testing. Samples with no shRNA treatment did not have separate batches. Altered splicing patterns were determined as reported.[36]

CLIP analysis

Inline barcodes and unique molecular identifiers (UMIs) were moved to the read names by Cutadapt[65] (v. 1.8.1), which also removed adapter sequences, using the parameter –minimum-length 14. The clipped adapter sequences were TAC CCT TCG CTT CAC ACA CAA GGG GAA AGA GTG TAG ATC TCG GTG GTC GC and AGA TCG GAA GAG CGG TTC AGC AGG AAT GCC GAG ACC GAT CTC GTA TGC CGT CTT CTG CTT. The 3' ends of each read were then trimmed of UMIs by removing the number of bases in the reciprocal adapter's UMI from the read ends, using cutadapt. All mapping used STAR (v. 2.7.8a). Reads were mapped first to a genome created from the rDNA locus sequence (Genbank accession U13369.1) using EndToEnd alignment. Unmapped reads were then mapped to a genome of repetitive elements created from Dfam release 3.3, curated entries only, (https://www.dfam.org/releases/Dfam_3.3/families/)[77] mapping with the parameter EndToEnd and disallowing splicing. Unmapped reads were then finally mapped to the genome (gencode release v29 basic annotation), allowing clipping, and splicing. After combining mapped reads from the three indexes, UMItools, specifically umi_tools dedup (v. 1.0), collapsed read duplicates using the UMIs in read names. Subsequent format conversions to bedgraph, wig, and bigwig were accomplished using bedtools (v. 2.30.0). Reads were assigned to genes using htseq-count on deduplicated bam files and only considering exons, after which reads not mapping to an exon were mapped to introns.

HOMER motif discovery analysis

MACS2 was run to call peaks on genomic and transcriptomic mappings, with bam file inputs and without control bam files, using the parameters –nomodel -q 0.01 –bw 100. These outputs were first filtered to the top 30,000 most significant and peaks overlapping ncRNA were removed. Peaks in the genome were then filtered to remove those without a clear strand, specifically those without at least a 5-fold enrichment in one strand over the other. Chromosomes other than autosomes, X, Y and the mitochondrial genome were removed. Peaks with FDR>0.01 were excluded and the 10,000 peaks with the lowest FDR were taken for analysis. Exonic peaks were defined as those overlapping with an exon by at least 40% of their length. Control sequence files were a minimum of 20,000 sequences created as random bases length-matched to the peak lengths. The findMotifs perl script in HOMER was called to search for motifs of length 6-8 with the parameters -rna and -homer1. Poly(U) and poly(S) sequences were found as background motifs in the CLIP-seq datasets in general with this approach.

QUANTIFICATION AND STATISTICAL ANALYSIS

Statistical analysis of biological data

All results are presented as the mean with SD unless notified specifically. Statistics were assessed using a Mann-Whitney U-test [motif enrichment], two tailed student t-test or Welch's t-test [general comparison], Audic and Claverie test [intron retention analysis], Fisher's exact adjusted by Benjamini/Hochberg [gene overlap]. All the GO analysis and Kyoto Encyclopedia of Genes and Genomes (KEGG) pathway analysis were performed with Enrichr and all the adjusted *p*-values for GO analysis were exported from Enrichr.[78–80] Markers of significance are as follows: #, $p > 0.05$; *, $0.01 < p \leq 0.05$; **, $0.001 < p \leq 0.01$; ***, $p \leq 0.001$.

Supplemental figures

CellPress
OPEN ACCESS

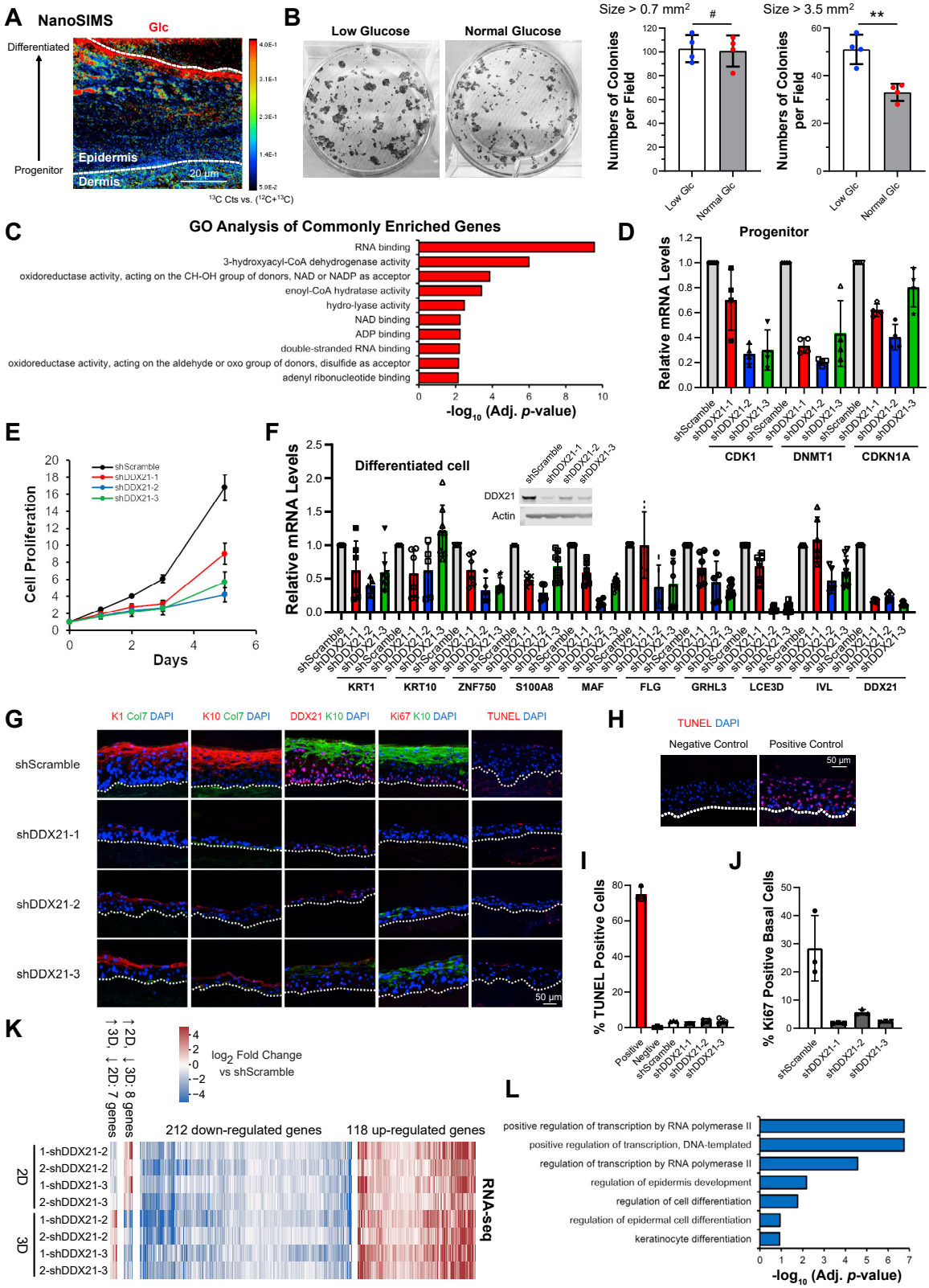

(legend on next page)

Figure S1. Glucose binds DDX21 and DDX21 is essential for epidermal differentiation, related to Figure 1

(A) NanoSIMS analysis of ^{13}C in skin tissue organoids cultured with $^{13}C_6$ glucose. Lower dotted line, the epidermal basement membrane; upper line, the outer differentiated granular layer.

(B) Colony formation of undifferentiated keratinocytes maintained in normal and low glucose media for 4 days before harvesting cells.

(C) GO analysis of the 91 proteins enriched in both the dextran column and azido glucose purification.

(D) qPCR of progenitor markers in progenitor cells after DDX21 knockdown, normalized to scrambled shRNA control.

(E) CTB assay of the cell proliferation rate of keratinocyte progenitor cells after DDX21 knockdown.

(F) qPCR of progenitor and differentiation markers in differentiated cells after DDX21 knockdown. Insert: western blot of DDX21 knockdown cells versus scrambled shRNA control.

(G) Organotypic human epidermal tissue comparing shDDX21 knockdown with shRNA control, stained for Keratin 1 (K1), Keratin 10 (K10), DDX21, Ki67, Collagen VII (Col7), or by the TUNEL assay. Dotted line, the basement membrane.

(H) Immunofluorescence images for TUNEL assay controls.

(I) Percentage of TUNEL positive cells for controls, shScramble and shDDX21 cells.

(J) Percentage of Ki67 positive cells among basal cells in shScramble and shDDX21 cells.

(K) RNAs that are commonly or differentially regulated in cultured differentiated keratinocytes and organotypic human epidermal tissues after DDX21 knockdown, from RNA-seq.

(L) Adjusted p values of biological process GO terms for those RNAs downregulated in cultured differentiated cells (512 genes from Figure 1F).

Error bars, standard deviations from $\geq$3 biological replicates. p values, two-tailed Student's t test.

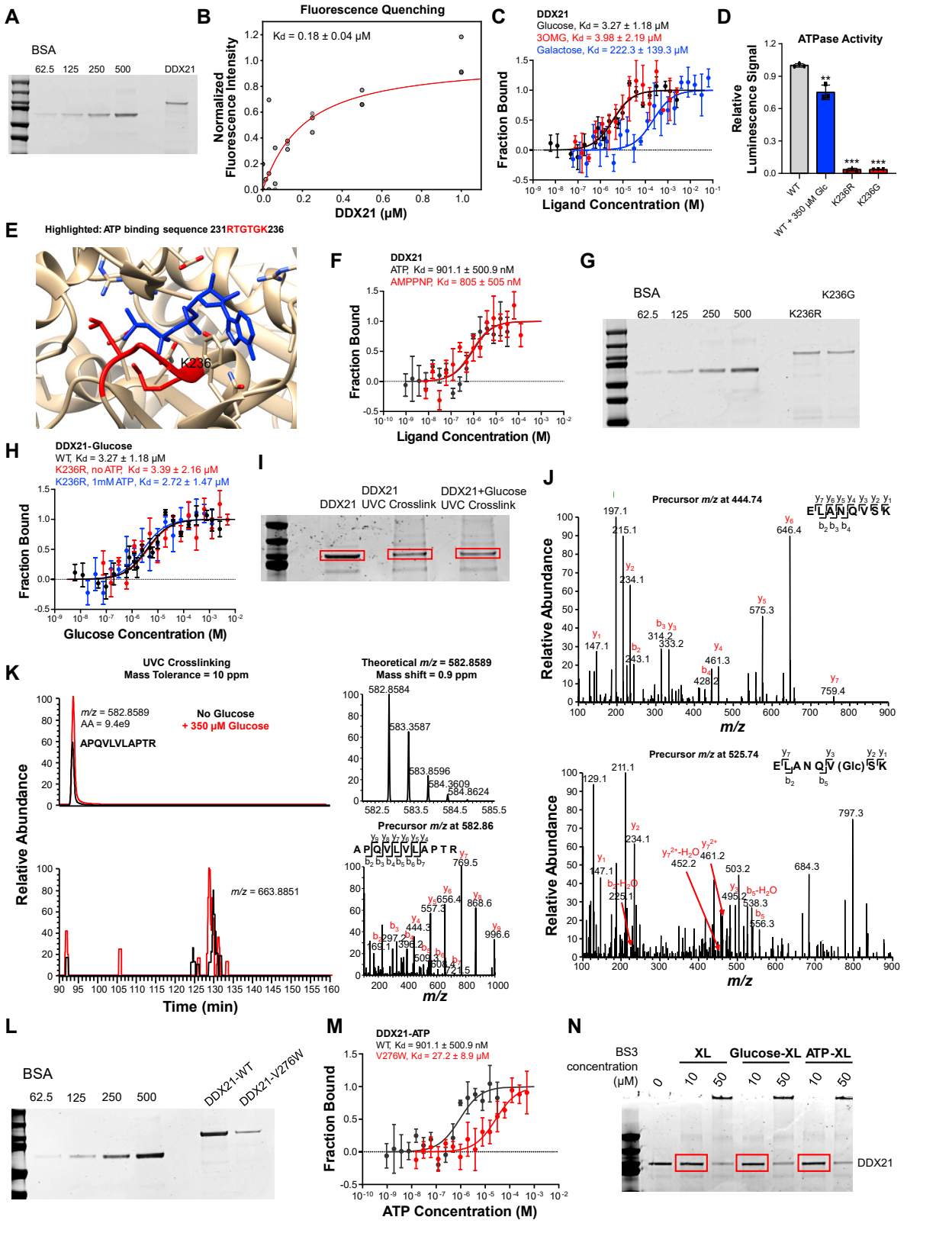

(legend on next page)

Figure S2. Glucose binds the DDX21 ATP binding site and changes DDX21 conformation, related to Figure 2

(A) SDS-PAGE of purified recombinant DDX21 protein.
(B) Fluorescence quenching analysis of binding between DDX21 and AZDye488-conjugated glucose.
(C) MST of the affinities of DDX21 for glucose, 3OMG and galactose.
(D) The ATPase activity of WT DDX21 ±350 μM glucose, or K236R/K236G mutants.
(E) The structure of AMPPNP bound to DDX21 (PDB: 6L5N).
(F) MST of the affinities of DDX21 for ATP or AMPPNP.
(G) SDS-PAGE of purified recombinant DDX21 K236R/K236G mutant proteins.
(H) MST of the glucose affinities to $DDX21^{K236R}$ ±1 mM ATP.
(I) SDS-PAGE of DDX21 before and after UVC crosslinking ±350 μM glucose. The bands in red boxes were subjected to in-gel digestion and mass spectrometry analysis.
(J) MS/MS of the un-crosslinked (top) and glucose crosslinked (bottom) DDX21 peptide (ELANQVSK), with (bottom) or without (top) incubation with glucose.
(K) SIC, MS, and MS/MS of the control DDX21 peptide (APQVLVLAPTR), with or without incubation with glucose.
(L) SDS-PAGE of purified recombinant WT and V276W mutant DDX21 proteins.
(M) MST of the affinities of ATP for WT DDX21 and $DDX21^{V276W}$.
(N) SDS-PAGE of DDX21 before and after BS3 crosslinking ±1 mM ATP or 350 μM glucose. The bands in red boxes were subjected to in-gel digestion and mass spectrometry analysis.
Error bars, standard deviations from ≥3 biological replicates.

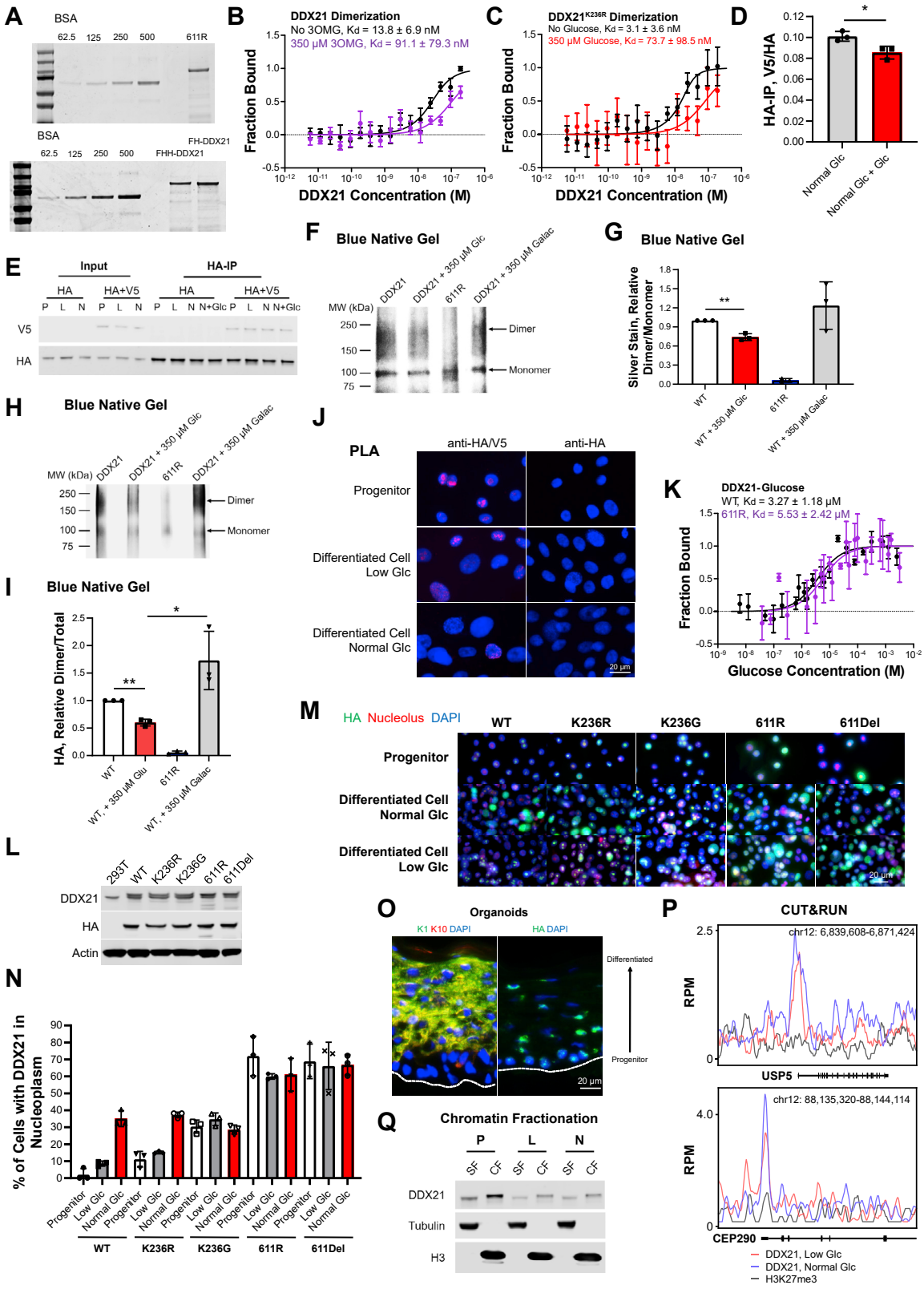

(legend on next page)

Figure S3. Glucose inhibits DDX21 dimerization and re-localizes DDX21 to the nucleoplasm, related to Figure 3

(A) SDS-PAGE of purified recombinant FHH-DDX21, FH-DDX21, and FHH-DDX21^{611R} proteins.

(B) MST of DDX21 dimerization ±350 μM 3OMG.

(C) MST of the binding affinities between FHH-DDX21^{K236R} and FH-DDX21 ±350 μM glucose.

(D) The V5/HA ratio from the co-immunoprecipitation of HA-DDX21 in differentiated keratinocytes maintained in normal glucose, with or without adding extra 350 μM glucose in the IP buffer, as quantified from western blot analysis.

(E) Western blot of the co-immunoprecipitation of V5-DDX21 by HA-DDX21 in keratinocyte progenitors (P) and differentiated cells grown in low (L) or normal glucose (N), with or without adding extra 350 μM glucose in the IP buffer.

(F) Silver staining of a blue native gel of DDX21 with or without 350 μM glucose or galactose incubation.

(G) The dimer/monomer ratio of DDX21 ±350 μM glucose or galactose from silver staining of blue native gels.

(H) Anti-HA western blot of a blue native gel of FHH-DDX21 proteins ±350 μM glucose or galactose.

(I) The dimer/total ratio of DDX21 with or without 350 μM glucose or galactose incubation from western blot. Total, western blot intensity above 80 kDa.

(J) PLA for the interaction of FHH-DDX21 and V5-DDX21 (dimerization) in progenitors and differentiated cells maintained in low or normal glucose.

(K) MST of DDX21^{611R} binding to glucose.

(L) Western blot of WT and mutant DDX21 expression levels in HEK293T cells.

(M) Immunofluorescence of the localization of DDX21 WT, K236R, K236G, 611R, and 611Del in keratinocytes under the indicated condition.

(N) Percentage of keratinocytes with nucleoplasmic DDX21 for DDX21 WT, K236R, K236G, 611R, and 611Del in keratinocytes under the indicated condition.

(O) Keratin 1 (K1), Keratin 10 (K10) and HA staining in organotypic human epidermal tissue with FHH-DDX21 expressed at endogenous levels. Dotted line, the basement membrane.

(P) DDX21 CUT&RUN binding at example loci of *USP5* and *CEP290*.

(Q) Western blot analysis of DDX21 in cell fractions in progenitor (P), differentiated keratinocyte grown in normal (N) and low glucose (L). SF, soluble fraction; CF, chromatin fraction.

Error bars, standard deviations from ≥3 biological replicates. p values, two-tailed Student's t test.

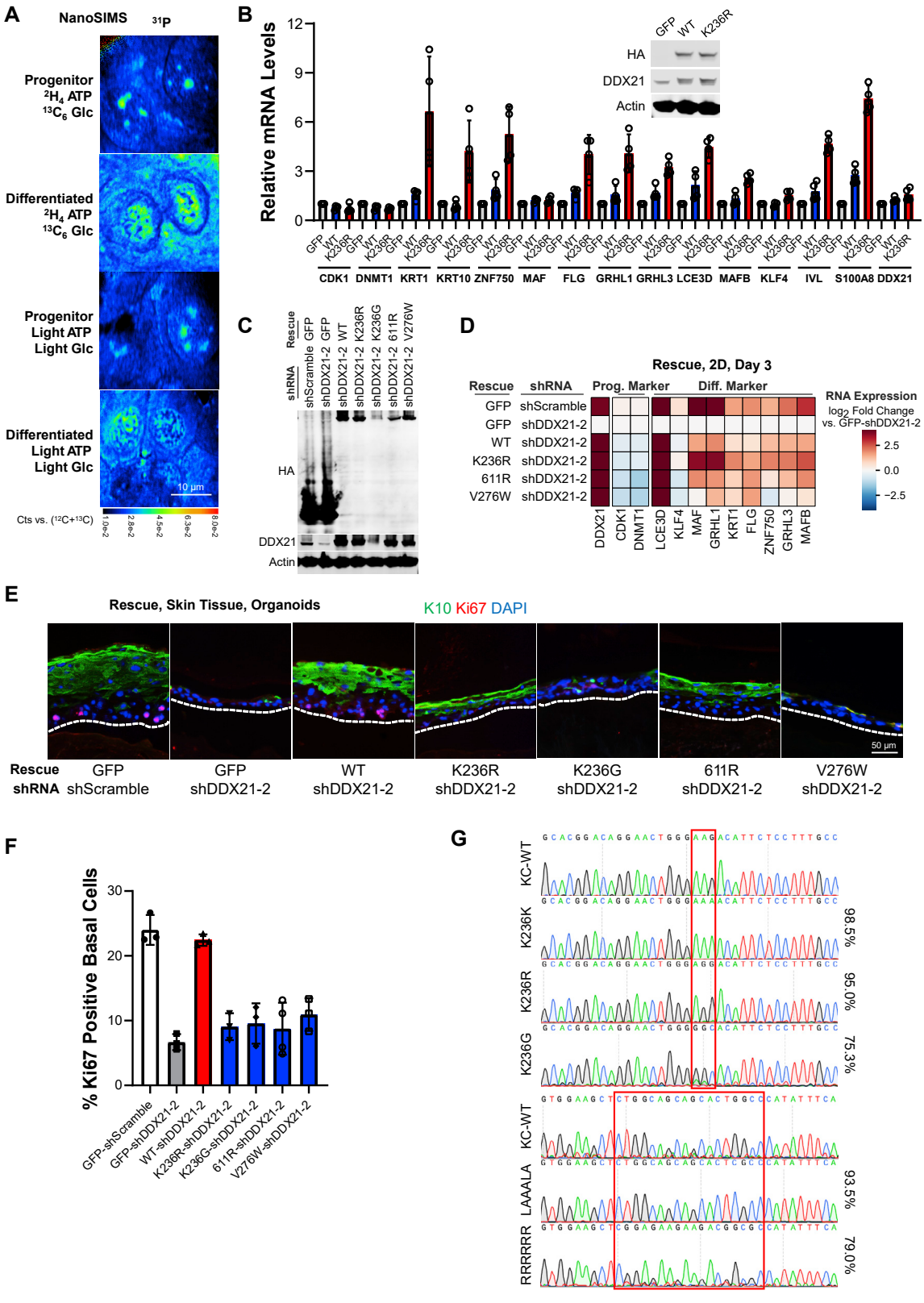

(legend on next page)

Figure S4. DDX21 enabled epidermal differentiation is ATPase-independent and requires glucose binding, related to Figure 4

(A) NanoSIMS of ^{31}P in progenitor and differentiated cells cultured with $^{13}C_6$ glucose and $^{2}H_4$ ATP (top two panels) or light glucose and ATP (bottom two panels). Intensities represent the relative counts normalized to total carbon counts ($^{12}C+^{13}C$).

(B) qPCR of progenitor and differentiation markers in keratinocyte progenitor cells after overexpression of DDX21 WT and K236R. Data normalized to GFP control. Insert: western blot of the enforced expression of DDX21 WT and K236R.

(C) Western blot of the enforced expression WT and mutant DDX21. GFP and DDX21 proteins were HA-tagged.

(D) qPCR of progenitor and differentiation markers in differentiated keratinocytes treated with control shRNA, DDX21 shRNA with GFP mock rescue, and DDX21 shRNA with WT or mutant DDX21 rescue. Data represent the mean values from ≥ 2 biological replicates. Data are normalized to DDX21 shRNA with GFP control.

(E) Staining of Keratin 10 (K10) and Ki67 in organotypic human epidermal tissue, comparing DDX21 shRNA with control shRNA, and DDX21 shRNA with WT or mutant DDX21 rescue. Dotted line, the epidermal basement membrane.

(F) Percentage of Ki67 positive keratinocytes among basal cells in shScramble and shDDX21 treated cells, with or without WT or mutant DDX21 rescue.

(G) Sanger sequencing chromatogram of targeted editing sequence at the endogenous *DDX21* gene locus; editing efficiencies are noted at right for each edit. The sequences highlighted in the red box are the edited sequences or the corresponding wild type (WT) sequences.

Error bars, standard deviations from ≥ 3 biological replicates.

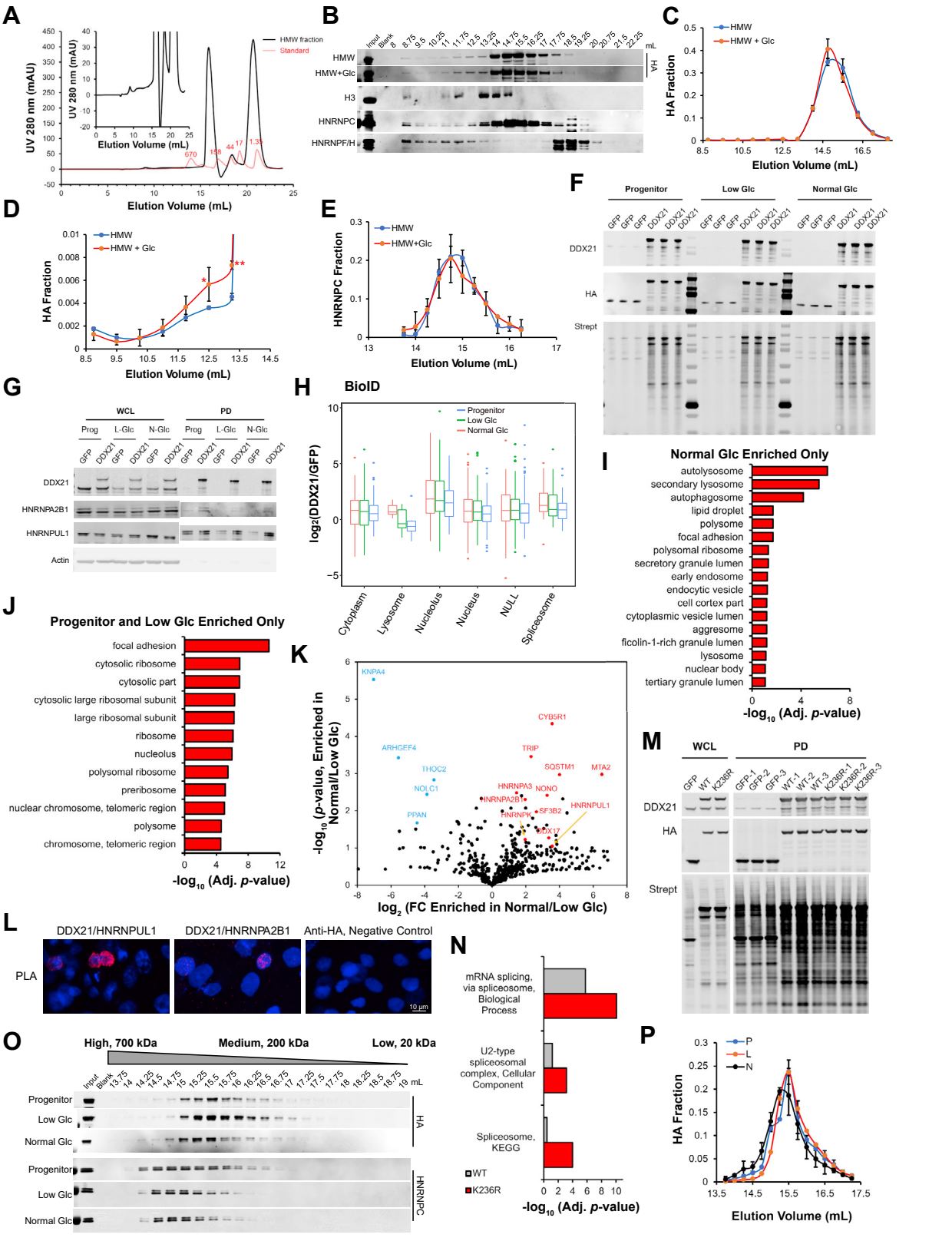

(legend on next page)

Figure S5. Glucose transitions DDX21 into a larger complex containing RNA splicing factors, related to Figure 5

(A) FPLC traces of the HMW fraction of HEK293T cells and gel filtration standard. The numbers in red are the molecular weight (kDa) of the corresponding peaks in FPLC.

(B) Western blot of DDX21 ±350 μM glucose in FPLC, in the HMW fraction. HNRNPC, histone H3 and HNRNPF/H are controls in the HMW fraction without glucose incubation.

(C) Distribution of DDX21 in FPLC from 8.75 to 17.75 mL in the HMW fraction from western blot.

(D) Narrower range of fractions quantitating DDX21 by western blot. The p value was calculated against the same elution volume of DDX21 without glucose incubation.

(E) Distribution of HNRNPC in DDX21 FPLC, from 13.75 to 17 mL, ±glucose in the HMW fraction from western blot.

(F) Western blot analysis of BioID samples in progenitor, differentiated cells maintained in low or normal glucose.

(G) Western blot of splicing factors in whole cell lysate (WCL) and BioID pull-down (PD) samples in progenitor, differentiated cells grown in low or normal glucose.

(H) Box and whisker plots of the enrichment of the indicated component in proximal proteomes from 472 enriched proteins. Whiskers, maximum and minimum ratios from BioID or 1.5 times the interquartile range. Boxes, interquartile range.

(I and J) Adjusted p values of cellular component GO terms enriched in DDX21 proximal proteomes in differentiated keratinocytes maintained in normal glucose only (n = 67) (I), or in progenitor and differentiated keratinocyte grown in low glucose only (n = 194) (J).

(K) Volcano plot of the enrichment in normal glucose over low glucose of the 472 enriched proteins.

(L) PLA for the interaction of FHH-DDX21 and V5-HNRNPUL1 or V5-HNRNPA2B1 in differentiated keratinocytes maintained in normal glucose.

(M) Western blot of WCL and BioID PD samples for WT DDX21 and DDX21^{K236R} in HEK293T cells.

(N) Adjusted p values of RNA splicing related biological process, cellular component GO terms and KEGG pathways enriched in DDX21 WT and K236R proximal proteomes in HEK293T cells.

(O) Western blot of HA-DDX21 and HNRNPC in FPLC of the HMW fraction in progenitor, differentiated keratinocytes maintained in low or normal glucose.

(P) Distribution of DDX21 in FPLC of the HMW fraction in progenitor cells, differentiated cells grown in low and normal glucose from western blot.

Error bars, standard deviations from ≥3 biological replicates. p values, two-tailed Student's t test.

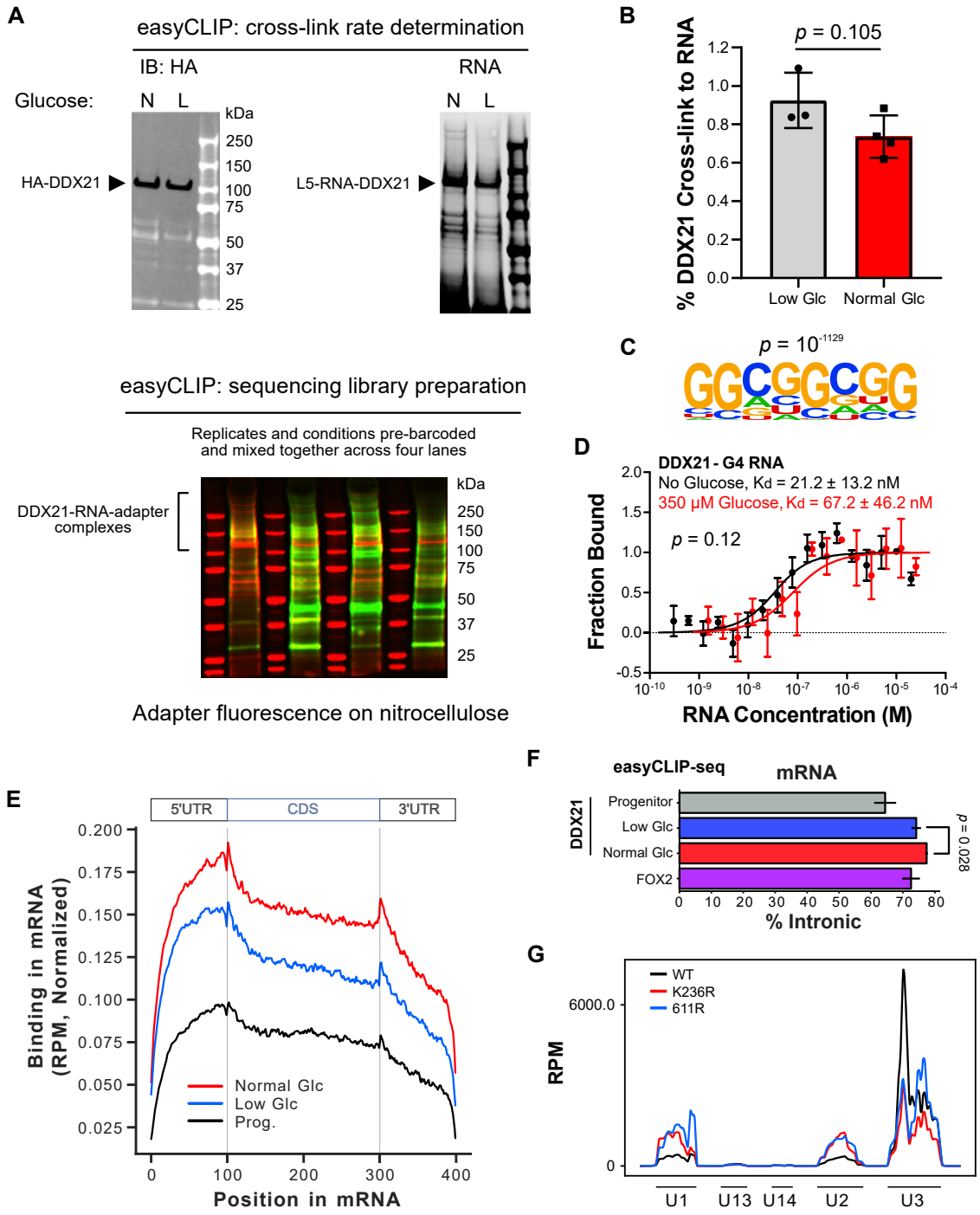

Figure S6. Glucose regulates DDX21 binding to RNA introns, related to Figure 6

(A) Fluorescence on nitrocellulose membranes for crosslinking rates determination (top) and sequencing library preparation (bottom) for easyCLIP of DDX21 in differentiated keratinocytes (N, normal glucose; L, low glucose).

(B) Percentage of DDX21 protein UVC-crosslinked to RNA under normal or low glucose conditions in differentiated keratinocytes.

(C) HOMER *de novo* searching of DDX21 CLIP-seq peaks in which intronic and exonic peaks were called separately.

(D) MST of purified DDX21 binding *in vitro* to a G4 RNA ±350 µM glucose.

(E) Length-normalized binding of DDX21 to mRNA in keratinocyte progenitors, differentiated cell maintained in normal or low glucose.

(F) Percentage of DDX21 binding to introns of mRNA in easyCLIP-seq from progenitor, differentiated keratinocytes grown in normal or low glucose media.

(G) Binding of DDX21 WT (black), K236R (red) and 611R (blue) to indicated RNA in HEK293T cells. Signal is smoothed over a 10 bp window.

Error bars, standard deviations from ≥3 biological replicates. p values, two-tailed Student's t test. FOX2 is a splicing factor control.

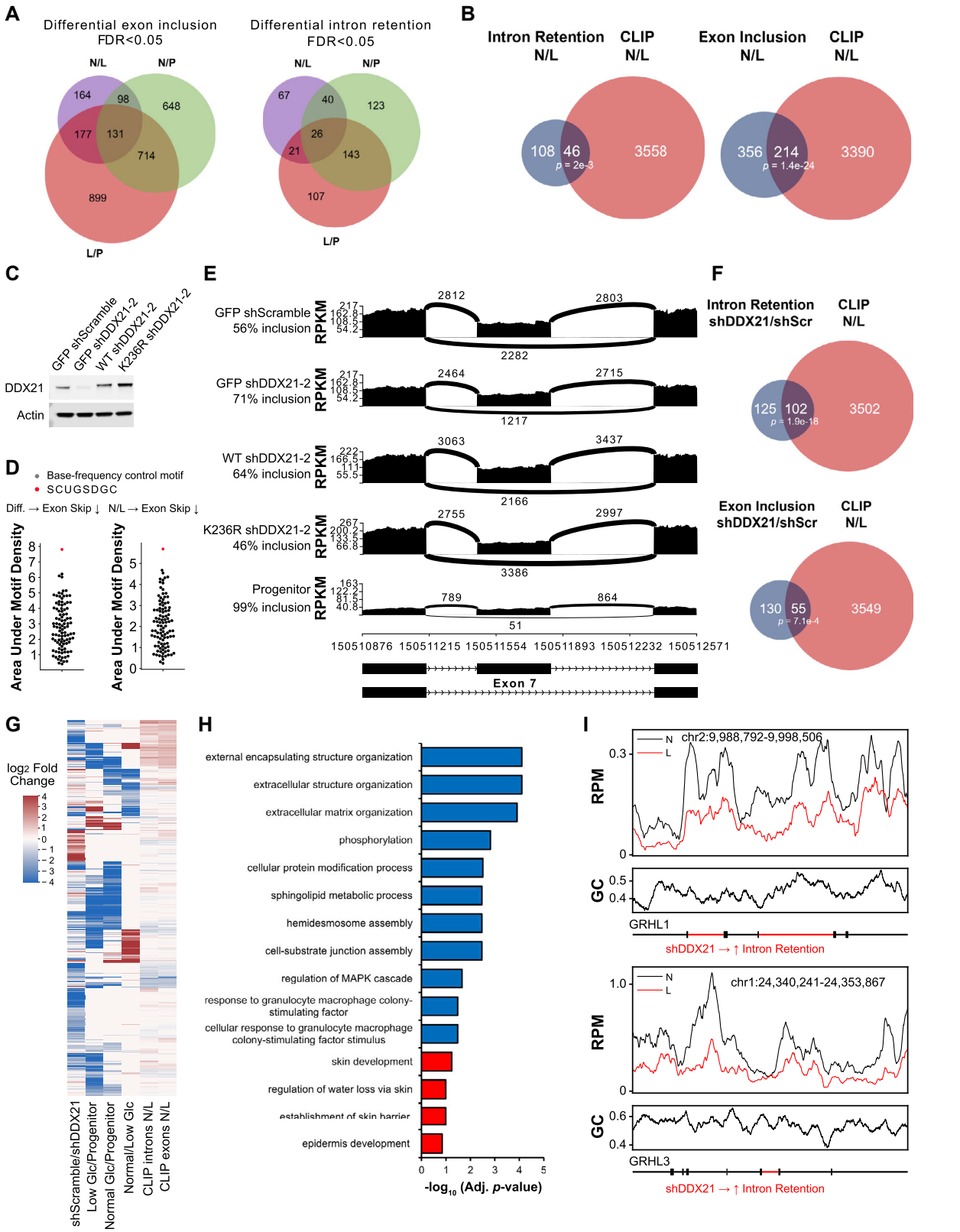

(legend on next page)

Figure S7. DDX21 regulates mRNA splicing, related to Figure 7

(A) Overlap of genes with differential exon inclusion (left) and intron retention (right) (Benjamini/Hochberg FDR < 0.05) among keratinocyte progenitors (P) and differentiated keratinocytes grown with either low (L) or normal (N) glucose levels.

(B) Comparison of RNAs bound by DDX21 (via CLIP) at different frequencies between keratinocytes grown in low or normal glucose levels with glucose levels-dependent differential intron retention (left) or exon inclusion (right).

(C) Western blot of the enforced expression WT and K236R DDX21 in the rescue experiment.

(D) A scatter plot of the area under the blue line in Figure 7D calculated for 100 random sequences, keeping the same length/nucleotide frequency/level of base degeneracy as SCUGSDGC. Red dot, SCUGSDGC motif.

(E) Sashimi plot of *ECM1* exon 7 skipping in the indicated conditions. Numbers over junctions indicate the number of junction-spanning reads.

(F) Comparison of RNAs bound by DDX21 (via CLIP) at different frequencies between keratinocytes grown in low or normal glucose levels with DDX21-dependent differential intron retention (upper) or exon inclusion (lower).

(G) Heatmap of the fold-change in intron retention across 533 differentially retained introns. Retained introns are FDR < 0.05 (Benjamini/Hochberg adjusted Audic and Claverie).

(H) Adjusted p values of biological process GO terms for those genes with DDX21-dependent intron retention and differential DDX21 easyCLIP-seq (102 genes from [F]).

(I) DDX21 binding across *GRHL1* and *GRHL3* mRNA near the retained introns. Curves are smoothed over a 500 nt window. The fraction GC is plotted as smoothed lines below in black.